

Additive manufacturing of a precious bulk metallic glass

Navid Sohrabi^{a,*}, Jamasp Jhabvala^a, Güven Kurtuldu^b, Ruggero Frison^c, Annapaola Parrilli^c, Mihai Stoica^b, Antonia Neels^c, Jörg F. Löffler^b, Roland E. Logé^a

^a Thermomechanical Metallurgy Laboratory, PX Group Chair, Ecole Polytechnique Fédérale de Lausanne (EPFL), 2002 Neuchâtel, Switzerland

^b Laboratory of Metal Physics and Technology, Department of Materials, ETH Zurich, 8093 Zurich, Switzerland

^c Center for X-ray Analytics, Swiss Federal Laboratories for Materials Science and Technology (Empa), Überlandstrasse 129, 8600 Dübendorf, Switzerland

ARTICLE INFO

Article history:

Received 6 February 2021

Accepted 20 May 2021

Keywords:

Additive manufacturing

Bulk metallic glass

Laser powder-bed fusion

Pd-based alloy

Selective laser melting

ABSTRACT

For the first time, a high-density amorphous and crack-free bulk metallic glass (BMG) based on a precious metal (PdCuNiP) was produced via additive manufacturing (AM). Laser powder-bed fusion (LPBF) was used for the fabrication of the samples, and led to a density of 99.6%. Excellent mechanical properties such as high hardness and compressive strength were achieved, overcoming the limitations usually found for precious metals in jewelry and watchmaking. Furthermore, without any post-processing, a mirror-like smooth and brilliant surface was directly obtained, which is highly beneficial for applications where surface finish or aesthetics matters. The effect of the main processing parameters, such as laser power and laser-scanning speed, on the shape of single tracks was investigated by laser confocal microscopy (LCM). Following the single-track experiments, highly amorphous LPBF samples were produced. The samples were characterized by optical microscopy (OM), scanning electron microscopy (SEM), conventional and synchrotron X-ray diffraction (XRD), micro-computed tomography (μ -CT), compression tests, and microhardness. The crystallization kinetics of the powder alloy was investigated via fast differential scanning calorimetry (FDSC). A small quantity of the powder (< 70 g) was used for the fabrication of samples, alleviating the cost of the process. Efficient production of precious metal parts with enhanced mechanical properties is demonstrated.

© 2021 The Author(s). Published by Elsevier Ltd.

This is an open access article under the CC BY-NC-ND license (<http://creativecommons.org/licenses/by-nc-nd/4.0/>)

1. Introduction

Precious metals have a variety of applications, especially in the watch and jewelry industries, related to their charming appearance, high corrosion and oxidation resistance, and non-allergic nature. Hardness and wear resistance are the two most important mechanical properties for the materials used in these sectors [1–4]. For example, a hardness higher than 300 HV is needed for watch components where wear and scratch resistance is required [5]. Since pure precious metals are soft and not resistant to wear and scratching, precious-metals-based alloys have been developed to obtain materials with improved (mechanical) properties. However, desirable mechanical properties in precious alloys are not easy to achieve, even after several thermo-mechanical treatments [2,6–9].

Bulk metallic glasses (BMGs) present a promising alternative to overcome the intrinsic limitations of their crystalline counterparts.

In fact, due to their amorphous structure, BMGs do not contain defects such as grain boundaries and dislocations. Therefore, they have enhanced properties such as high strength and hardness; exceptional wear, corrosion and oxidation resistance; and high elastic limit [10]. The first metallic glass was produced in 1960 based on gold [11]. Afterwards, BMGs based on other precious metals such as Pd [12], Pt [13], and Ag [14] were developed.

Pd-based metallic glasses are known as amorphous alloys that have a wide range of supercooled liquid region (SCLR) and high glass-forming ability [12,15,16]. These properties allow the fabrication of amorphous parts with diameters of up to 72 mm [17]. According to Lu et al. [18], the Pd-based metallic glass with the composition Pd₄₃Ni₁₀Cu₂₇P₂₀ has higher glass-forming ability than other similar compositions that are richer in copper [19].

One of the main obstacles to the widespread use of BMGs is the limited size and geometry of BMG parts produced with conventional methods such as casting [20,21]. If the size of the cast sample is larger than the critical casting diameter, the sample will undergo crystallization [22] and in most cases, it will form inter-metallic phases reducing the toughness drastically [23]. After cast-

* Corresponding author.

E-mail address: navid.sohrabi@epfl.ch (N. Sohrabi).

ing, thermoplastic forming (TPF) is also often required to produce near-net-shape parts [24,25], which further increases the fabrication time and the risk of crystallization [24].

Laser powder-bed fusion (LPBF), also called selective laser melting (SLM), is an additive manufacturing (AM) process that has attracted much attention in recent years. Advantages of this method include the ability to build complex shapes, minimal feedstock waste, mass-customized production and low lead time of production [26]. Because the layer thickness of the powder in the LPBF process is less than 100 μm , the energy required to melt the powder is lower and higher scanning speed can be implemented. Consequently, the size of the melt pool is smaller and the interaction between the laser and the powder is limited to a short time (tens of microseconds). Therefore, depending on the processing parameters, the local heating rate (R_h) and cooling rate (R_c) can reach 10^3 – 10^8 K/s [27,28]. The R_c in the LPBF process is typically higher than the critical cooling rate (CR_c) of most BMGs [10]. In theory it is, therefore, possible to suppress crystallization and manufacture amorphous metals after solidification [29,30]. Several BMGs based on Fe [20,22,31–39], Al [40–43], Zr [44–60,61], Cu [62,63], and Ti [64] have been manufactured via the LPBF process, but there is no report so far on precious BMGs based on Au, Pd, Pt or Ag manufactured with this method. Although Fischer et al. [65] were able to produce an amorphous Pt-based BMG by selective laser sintering (using a pulsed laser), the part was very porous due to partial melting of the powder particles.

The most important processing parameters in LPBF are laser power, scanning speed, layer thickness, and hatching distance [26]. Optimization of the mentioned parameters is required to manufacture a fully dense sample. Yadroitsev et al. [66] determined the processing parameters by printing single tracks, assuming that the properties of the final part depend on those obtained with single tracks. Bosio et al. [67] used the optimized parameters of single tracks for producing bulk samples and concluded that it is a time-saving and cost-effective method.

In the present study, a dense, crack-free, and highly amorphous Pd-based BMG is fabricated via LPBF for the first time. The printing parameters are determined using single line tracks. It is shown that high heat input leads to an increase in the average temperature of the sample and causes irregularities in the shape and geometry of the part. The mechanical properties of the manufactured parts, such as hardness and compressive yield strength, are investigated.

2. Materials and methods

A Pd-based metallic glass powder with a nominal composition of $\text{Pd}_{43}\text{Cu}_{27}\text{Ni}_{10}\text{P}_{20}$ (at%) was supplied by PX Group. The powder-particle size distribution ranges from 10 μm to 50 μm . LPBF experiments were carried out on an in-house laboratory LPBF station [68] with a 500 W fiber laser (wavelength of 1070 nm) and a spot size of 65 μm . During fabrication, nitrogen was used as a protective gas inside the working chamber. Substrates from bronze (CuSn–Ni–P) were deployed for printing the bulk samples. A scanning strategy of parallel lines (uni-directional) with an orientation change of 90° for each layer was used for all experiments.

The manufactured specimens were cut and ground with sandpapers (until grit 2500) and polished with a suspension of alumina particles until 1 μm size. The porosity content of the samples' X-Z cross-sections was measured by optical microscopy (OM) with a Leica DM6000M using the ImageJ® software. The microstructures and fracture surfaces were characterized with a ZEISS GeminiSEM450 Scanning Electron Microscope (SEM), equipped with an energy dispersive spectroscopy (EDS) device.

The crystallization kinetics of the powder particles were studied by fast differential scanning calorimetry (FDSC). Individual spherical powder particles with a size of approximately 20 μm in diame-

ter were placed onto the UFH1 sensor of a Mettler-Toledo FDSC 2+ device using an electrostatic manipulator. An Ar flow of 20 ml/min was applied to prevent sample oxidation during the measurements. The FDSC sample mass was determined using the melting enthalpy of the equilibrium state, solidified at a rate of 0.05 K/s and measured at a heating rate of 1000 K/s via FDSC, and that of the reported value (7.01 kJ/mole) [18] measured via conventional DSC, using the relation given in Refs. [69,70]. The time-temperature-transformation (TTT) diagram for the $\text{Pd}_{43}\text{Cu}_{27}\text{Ni}_{10}\text{P}_{20}$ powder alloy was obtained via FDSC, following a similar experimental procedure as reported in Refs. [71–75]. The temperature calibration for the FDSC measurements was performed by comparing the melting onsets of the equilibrium state solidified at a rate of 0.05 K/s and that reported by Lu et al. [18].

Micro-Computed Tomography (μ -CT) analysis was carried out on a cylinder with a diameter of 3 mm and height of 4 mm, using an EasyTom XL Ultra 230–160 micro/nano-CT scanner (RX Solutions, Chavanod, France) [61]. The scanner was operated at 200 kV and a current of 50 μA with an Al–Cu filter. The sample was scanned over 360° with a rotation step of 0.25° and a frame average of 10. The nominal resolution was set to 2.3 μm voxel size.

To check the possible content of crystalline phase/s, X-Ray Diffraction (XRD) experiments were performed with a Panalytical Empyrean diffractometer (Theta-Theta, 240 mm), equipped with a PIXcel-1D detector in reflection mode. In addition, synchrotron XRD experiments were performed on one selected sample at the X04SA Materials Science Beamline of the Swiss Light Source, Paul Scherrer Institute (PSI), using a wavelength of 0.5638 Å and the Mythen-II detector in transmission geometry. The thickness of the sample was ~120 μm . The data presented here has been corrected for extrinsic background and for sample absorption contributions using in-house developed software.

The oxygen content of the powder and manufactured samples was measured with a LECO OHN 836 analyzer using the carrier gas hot-extraction method. The average value of three measurements is reported. The calibration of the device was performed from steel calibration samples provided by LECO, after each measurement.

The microhardness tests (HV) were carried out using a Qness Q10A machine with 1 and 0.1 kg force (HV 1 and HV 0.1, respectively), and a dwell time of 10 s. The distance between two adjacent indents was at least three times the diameter of the indents.

Five cylinders with a height of 6 mm and diameter 4 mm (height-to-diameter ratio 1.5) were used for uniaxial compression tests. The tests were performed using a Gleeble 3800 machine at a strain rate of $1 \times 10^{-4} \text{ s}^{-1}$.

A VK-X1100 3D laser-scanning confocal microscope was used to study the samples' surface roughness and the shape of single laser tracks and printed parts.

3. Results and discussion

Fig. 1a shows the XRD pattern of the powder produced by gas atomization. The broad peak indicates that the powder is amorphous. SEM images of the powder are presented in Fig. 1b and c. The powder particles are spherical and appropriate for the LPBF process. Some porosities, shown by white arrows in Fig. 1c, are detectable in the cross-sections of the powder particles. These porosities were created during the gas-atomization process. The oxygen content of the powder was measured as 150 ± 25 ppm using the carrier gas hot-extraction method.

3.1. Single tracks

The quality of the fabricated parts relates to that of each laser track and each layer. To eliminate the effect of the substrate and the inherent problem of the first layer's non-uniform thickness,

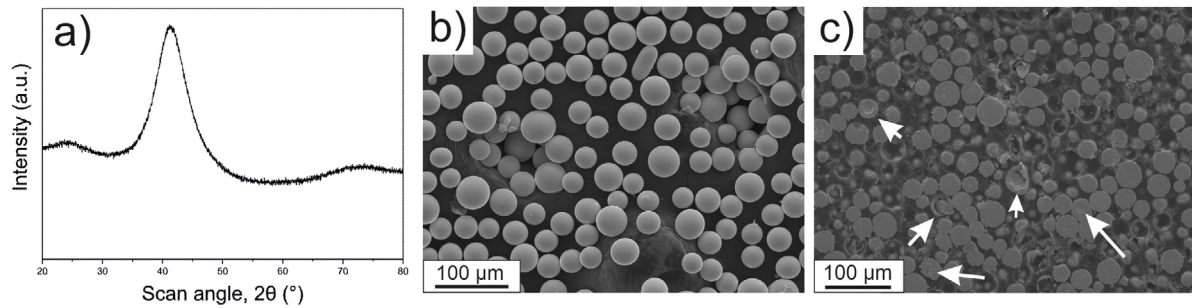


Fig. 1. (a) XRD pattern of the powder, (b) SEM image of the powder, and (c) SEM image of the cross-sections of the powder particles revealing the presence of porosity inside the powder particles.

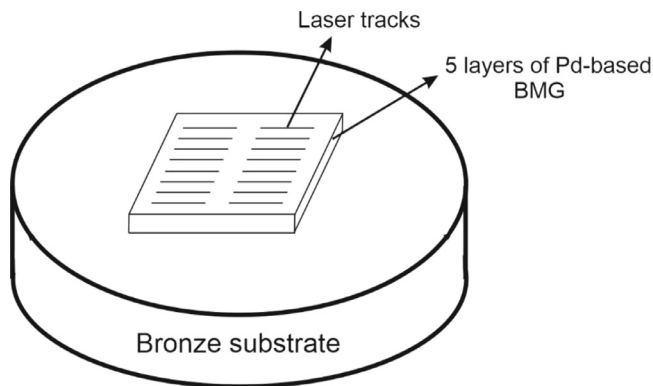


Fig. 2. Schematic view of the single-track experiments.

single tracks were fabricated after printing five layers of a Pd-based BMG cube with a size of $20 \times 20 \times 0.2 \text{ mm}^3$ (see Fig. 2). This approach has two more benefits; first, the thermal and physical properties of the single tracks and the substrate are the same; and second, the BMG substrate prevents quick heat dissipation (due to low conduction), and thus mimics better the real conditions operating when printing bulk samples.

Fig. 3 displays Laser Confocal Microscopy (LCM) images of the single laser tracks obtained with different processing parameters. The laser power varied from 20 W to 150 W for two scanning speeds, 600 and 1000 mm/s, while keeping the layer thickness constant at $40 \mu\text{m}$. The scanning direction was from right to left.

At 600 mm/s, the laser track produced with a laser power of 25 W (Fig. 3a) is not continuous. The power was too low and the laser could not melt the powder completely. Therefore, some disconnected metal beads were created, leading to the so-called balling effect [76,77]: at low power, the size and the peak temperature of the melt pool are reduced, while surface tension increases and prevents the wetting and coalescence of the beads. The molten material then minimizes the surface energy by evolving into spheres [78]. As the laser power increases, the shape instability decreases (Fig. 3e,g). The tracks produced with 40 W and 60 W are homogeneous in length and width. When the power increases to 80 W and higher, the width and the height at the end of the tracks are larger, resulting from a deceleration of the scanning head. At this point, the interaction time between the laser and the powder is longer due to an effective lower scanning speed [79,80], which results in an increase of the melt pool size. Using higher power while printing makes this problem even more pronounced. A similar trend can be seen for the tracks printed with a scanning speed of 1000 mm/s, but this time the instability at the end of the track is almost systematic. This is consistent with the work of Tian

et al. [80], in which the melt pool was found to be more unstable at higher scanning speed.

A comparison of the height and width of the laser tracks is presented in Fig. 4. Values are higher at 600 mm/s as a consequence of a higher volume energy density (VED). In general, an increase in laser power leads to wider tracks and slightly increased heights.

3.2. Bulk samples

The average width of the laser tracks fabricated with a scanning speed of 600 mm/s is $276 \mu\text{m}$. To have almost 50% overlap between adjacent tracks, a hatching distance of $150 \mu\text{m}$ was chosen for the fabrication of bulk samples. The same hatching distance was used for the samples fabricated with a scanning speed of 1000 mm/s, for ease of comparison.

The Volume Energy Density (VED) is expressed in the standard way:

$$\text{VED} = \frac{\alpha P}{v h L},$$

where α is the material absorptivity, P the laser power (in W), v the laser speed (m/s), h the hatching distance (m), and L the layer thickness (m). The absorptivity of the liquid was set to 0.28 from theoretical calculations based on electrical resistivity, as explained in Ref [81]. It is now known that VED is not the best design quantity to compare different materials or to correlate them with melt-pool geometry or defect content, because of the absence of material-related parameters [82,83]. Other concepts such as the Normalized Enthalpy have been shown to be more effective, in particular with respect to determining the material's heat diffusivity [84,85]. Nevertheless, the VED approach has been used here for the purpose of comparing samples of the same composition and because it reveals the total energy density received by the sample, taking into account hatching and layer thickness, which both are important parameters when dealing with heat accumulation. The normalized enthalpy, on the other hand, gives a local energy density on a cylinder defined by the diameter of the laser spot and a thermal length [84].

Twelve samples with a size of $5 \times 5 \times 1 \text{ mm}^3$ were fabricated using the parameters given in Table 1. Fig. 5 shows the top surfaces of the samples. High VED led to irregular shapes and wavy surfaces (see white arrows). The probable reason of the samples' irregular shape is the increase in the average sample temperature. Using high power for fabrication keeps the temperature at a high level, and the material has thus not enough time to cool to room temperature between successive adjacent laser tracks. The accumulation of heat increases the average temperature which, when exceeding the glass transition temperature (T_g), renders the material soft and viscous.

To confirm the above hypothesis, a sample with the same processing parameters as used for sample 2 was fabricated, but a

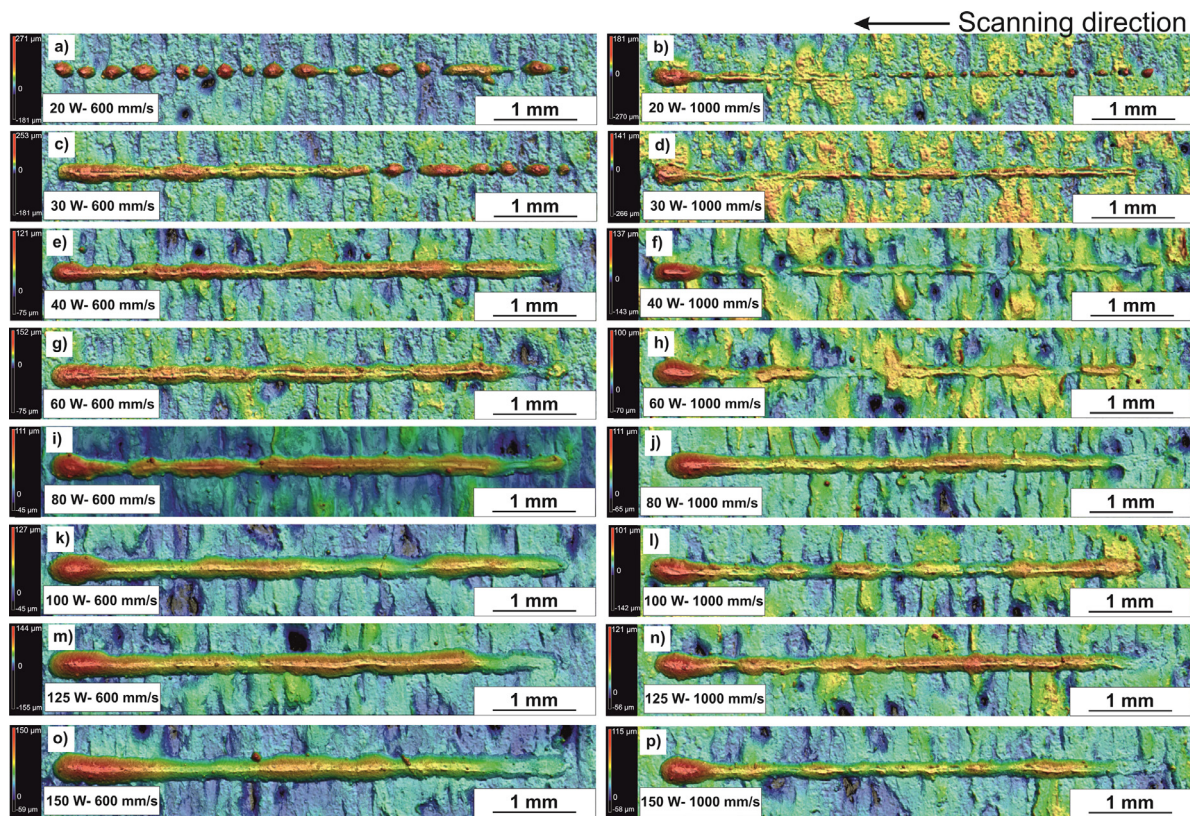


Fig. 3. Laser confocal microscopy (LCM) images of single laser tracks at 600 mm/s (left) and 1000 mm/s (right) scanning speeds. The scanning direction is from right to left.

Table 1

Processing parameters used for the fabrication of bulk samples and finding the optimized condition. Despite of not having the highest density, the processing parameters for sample 4 (bold) were most optimized to produce a regularly shaped sample (see Fig. 3g and Fig. 5).

Sample	Power (W)	Scanning speed (mm/s)	Hatching distance (μm)	Layer thickness (μm)	VED (J/mm^3)	Density (%)
1	150	600	150	40	11.7	–
2	100	600	150	40	7.8	99.90
3	80	600	150	40	6.2	99.48
4	60	600	150	40	4.7	99.63
5	40	600	150	40	3.1	98.36
6	20	600	150	40	1.6	–
7	150	1000	150	40	7.0	–
8	100	1000	150	40	4.7	99.76
9	80	1000	150	40	3.7	99.73
10	60	1000	150	40	2.8	99.53
11	40	1000	150	40	1.9	99.16
12	20	1000	150	40	0.9	–

waiting time of 1 second was added between each adjacent laser track, to make sure that the overall sample temperature remained well below T_g . Printing one laser track with 5 mm length and a scanning speed of 600 mm/s takes 8 ms. Fig. 6a and b show 3D confocal images of the samples without and with waiting time, respectively, and Fig. 6c presents a height profile of a line on the top surface of the samples. The shape of the sample without waiting time (Fig. 6a) resembles a drop of liquid on a surface. The sample with waiting time shows a more regular and flat shape compared to the previous one. However, some irregularities can still be detected at the edges of the sample, which may be attributed to the deceleration of the scanning head at the end of the track, consistent with the instabilities identified in Fig. 3. When the next powder layer is deposited, the amount of powder varies spatially according to the height profile, and so does the local VED [86]. Less powder means increased VED and thus a larger melt pool, potentially causing humping [87].

For samples 6 and 12, the VED was not high enough to completely melt and consolidate the powder, leading to high porosity. As can be seen in Fig. 5 (see black arrow), a part of sample 6 was even removed due to a loose bonding among the sintered powder particles.

Some of the parameters used for single tracks, such as very low (20 W) and very high powers (150 W), were used for printing bulk parts, although they did not result in continuous or stable tracks, respectively. This was done to illustrate the connection between the quality of the tracks and that of the final product. It can be seen in Fig. 5 that non-continuous tracks did not produce dense bulk parts and that tracks with an instability at the end resulted in parts with irregular shapes.

Fig. 7 presents optical images of the cross-sections of some samples that were produced by the parameters given in Table 1. The samples produced with a power of 40 W and 60 W have more regular shapes. As power increases, the surface becomes curved

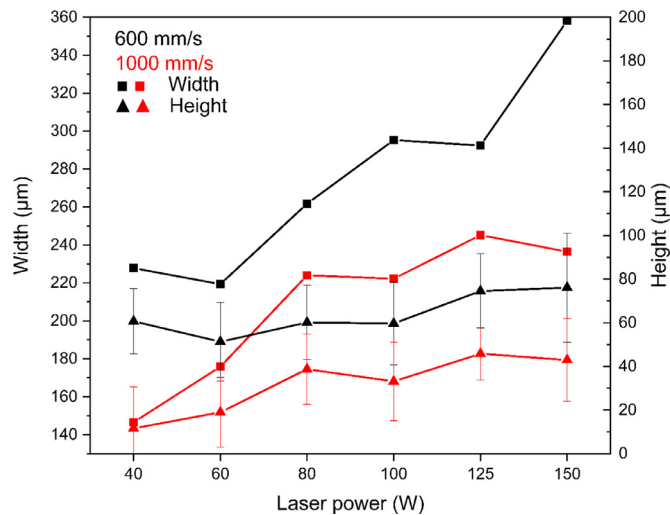


Fig. 4. Comparison of the width (squares) and height (triangles) of the single tracks produced with scanning speeds of 600 mm/s (in black) and 1000 mm/s (in red).

and irregular, and thus reduces the accuracy of the part. Cross-sections obtained with a power of 150 W are not shown because the shape changes are even worse than for those obtained at 100 W.

The porosity content of the samples' cross-section was measured by image analysis (software ImageJ®). The results are given in Table 1. The four samples with the lowest amount of poros-

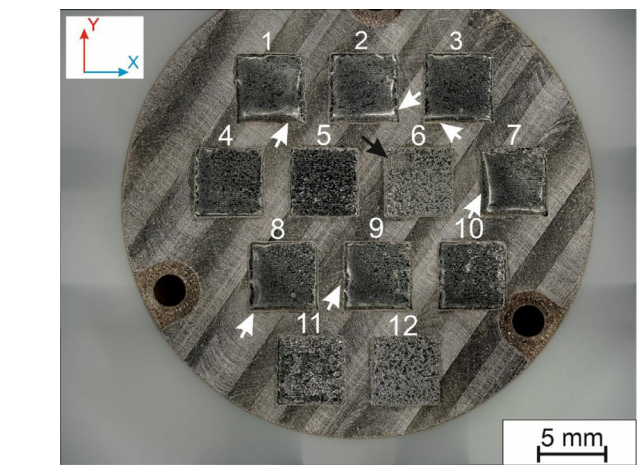


Fig. 5. Samples fabricated using the processing parameters given in Table 1 (top view, X-Y). A too high VED led to irregular shapes and wavy surfaces (see white arrows) and a too low VED did not completely melt and consolidate the powder (see black arrow).

ity are samples 4, 9, 8 and 2, respectively. Although sample 4 had the highest porosity content (0.37% area fraction) among these samples, it was selected as the optimized one from a manufacturing point of view because of its regular shape. The corresponding set of processing parameters corresponds to one of the two best results for single tracks (see Fig. 3e and g). This result highlights the importance of optimizing the processing pa-

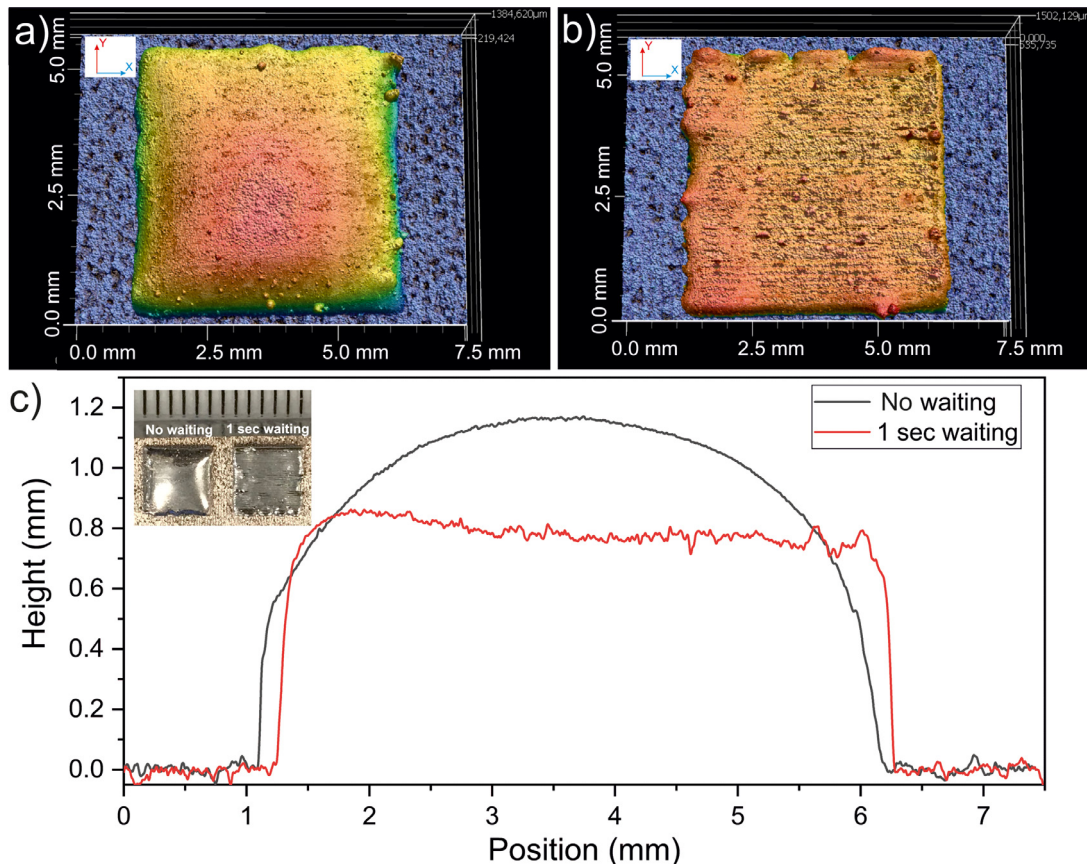


Fig. 6. 3D confocal image of sample 2, (a) without waiting time and (b) with 1 second waiting time after each laser track. (c) Height profiles of a line on the samples' top surface for cases a) and b). The inset in c) shows the real samples.

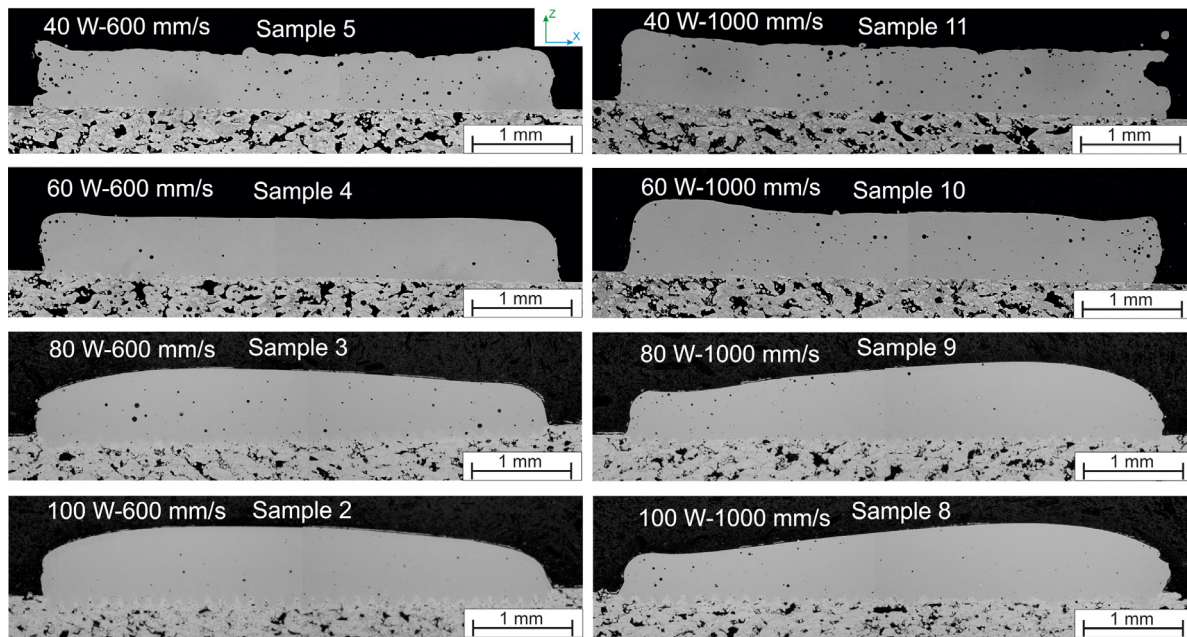


Fig. 7. Optical microscopy (OM) of X-Z cross-sections of eight samples produced with the processing parameters given in Table 1.

rameters by printing single tracks and then achieving a reasonable density.

We can compare the VED values to the material volumetric heat of fusion, i.e. the energy density needed to melt the material in an ideal case with no loss. This value is calculated as 3.55 J/mm^3 from the measurements of Ref. [88]. The best densities (lowest porosity content) identified earlier all have a VED above this value. Lower VED values result in higher porosity, and much larger values lead to irregular shapes.

The comparison of VED and volumetric heat of fusion can give a first reasonable approximation of processing parameters, but this alone may not be enough to accurately classify sample quality. This is illustrated by sample 7, which reveals an irregular shape although its VED is smaller than that of sample 2.

Samples 1, 2 and 4 were selected for XRD tests. The top surface of the samples (X-Y cross-section) was first ground with sandpapers (until grit 2500) such as to remove about $200 \mu\text{m}$ of surface material. In addition, X-Z cross-sections of the samples were prepared by cutting the samples and grinding almost $100 \mu\text{m}$ from the bottom of the sample to remove any effect of dilution with the substrate. XRD tests were then performed, with the results shown in Fig. 8. The XRD patterns of samples 1, 2 and 4, produced with 150 W, 100 W and 60 W, respectively, show a broad symmetric peak indicating an amorphous structure (within the detection limit of the XRD test). Although it was shown that the processing parameters of sample 2 led to an increase in the average sample temperature, it did not cause detectable crystallization by XRD. It seems that this alloy, unlike Zr-based BMGs [59], can retain an amorphous structure for a wide range of VED (wide processing window) and is not very sensitive to an increase of heat input. This relates to the good GFA of Pd-based BMGs [12,15,16], i.e. they can withstand long time and/or high temperatures without undergoing extensive crystallization.

The parameters used for manufacturing sample 4 are considered as optimized because it has a regular shape, a relatively low amount of porosity (less than 0.4%), and an XRD amorphous structure. The next section is dedicated to in-depth characterizations and mechanical properties of the optimized sample (sample 4).

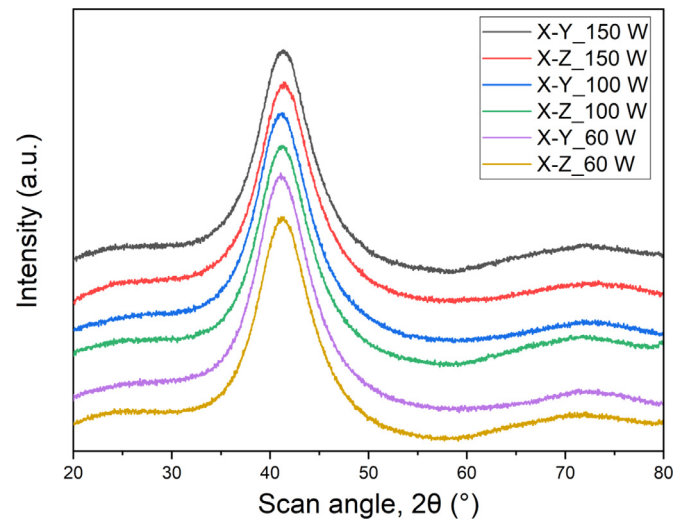


Fig. 8. XRD patterns of printed samples from two cross-sections, X-Y ($200 \mu\text{m}$ below the top surfaces) and X-Z, produced with a scanning speed of 600 mm/s , hatching distance of $150 \mu\text{m}$ and layer thickness of $40 \mu\text{m}$.

3.3. Optimized processing parameters

The oxygen content of the fabricated sample was $25 \pm 5.5 \text{ ppm}$. Unlike Zr-based BMGs [61], the oxygen content of the Pd-based BMG fabricated via LPBF is lower than the value of the virgin powder. The reason is that oxygen is interstitially dissolved in the Pd-based BMG because Pd is not inclined to form oxides with oxygen, which then gives the possibility for oxygen to escape the material during LPBF.

The surface roughness S_a of the sample was measured by confocal microscopy, with a value of $1.35 \mu\text{m}$. Without any post-processing, a liquid-like smooth and brilliant surface was directly achieved.

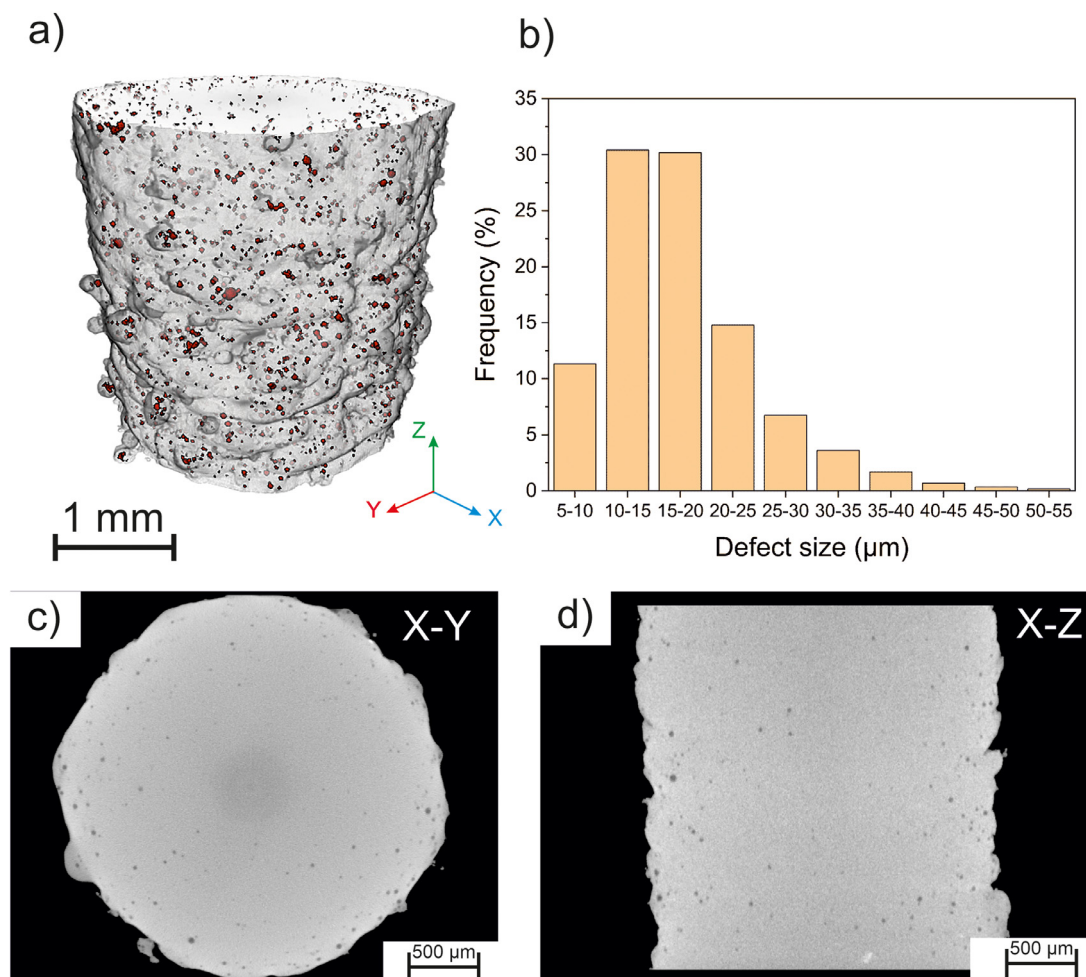


Fig. 9. μ CT results of a cylinder with 3 mm diameter and 4 mm height, produced with the optimized LPBF parameters. (a) 3D image of the sample, with defects shown in color; (b) histogram of the defect size distribution; (c) snapshot of X-Y cross-section; and (d) snapshot of X-Z cross-section.

3.4. Characterization of the optimized bulk sample

Fig. 9 presents μ CT results of a cylinder with a diameter of 3 mm and height of 4 mm, produced with the optimized parameters. The volume fraction of porosities inside the sample was 0.4%. Although this value is very close to the previously measured area fraction of porosities in sample 4 (0.37%, see Table 1), it might be slightly underestimated because of the nominal resolution of the μ CT scan. Fig. 9b reveals the defect size distribution with a maximum in the 10–20 μ m range, and an upper bound at 55 μ m. Fig. 9c and d show two snapshots of X-Y and X-Z cross-sections.

Although Fig. 8 indicates that sample 4 is amorphous, crystallization was detected at the interface of the Pd-based BMG and the bronze substrate (see Fig. 10). The reason for crystallization is the intermixing of the printed material and the substrate [60], with a chemical composition change at the origin of crystallization. Fig. 10c reveals that the crystals have nanometric size, and EDS analysis (see Fig. 10d-h) shows that they are rich in Cu and poor in Pd and P (compared to the amorphous matrix). Such a change in the chemical composition was also observed in Ref. [19] during the crystallization of a $\text{Pd}_{40}\text{Cu}_{30}\text{Ni}_{10}\text{P}_{20}$ glass at temperatures near the nose of the TTT diagram. In addition, Sn is also detected in the crystallized region, which most likely diffused from the substrate. The intermixing occurred only in the first layer of the sample and this region can be easily removed when cutting the sample from the substrate.

The shape of porosities can give information about their creation mechanism. For instance, if it is irregular, it may be due to a lack of fusion (LoF). In sample 4, the shape of porosities is spherical (see Fig. 7), which may correspond to gas entrapment during LPBF or atomization of the powder. Fig. 1c shows an SEM image of the polished cross-section of the powder particles. Particles shown by white arrows were hollow and contained an initial porosity, which may be difficult to remove by laser melting.

Following Shen et al. [89], elemental vaporization during laser processing can happen for the elements with high vapor pressure. This may create porosity and accelerate crystallization due to local chemical composition changes. In this study, phosphorus is the element most prone to vaporization. An EDS analysis close to a pore (see Fig. 11) shows, however, a uniform distribution of all elements. Besides, there is no evidence of crystals with a change in phosphorus content (see Table 2).

Marattukalam et al. [59] investigated LPBF of a Zr-based BMG. Using TEM, they showed that although conventional XRD did not reveal any sharp peaks, nanocrystals still formed during laser processing. This is consistent with our previous works [60,61]. To investigate in more detail the structure of sample 4, a thin lamella (thickness ~ 120 μ m) was extracted 200 μ m below the top surface in the X-Y plane (see inset of Fig. 12a). The sample was ground with sandpaper until a mesh size of 2500. Diffraction patterns at eight different locations were collected using synchrotron X-ray radiation. The high photon flux ensures a sensitive detection of crys-

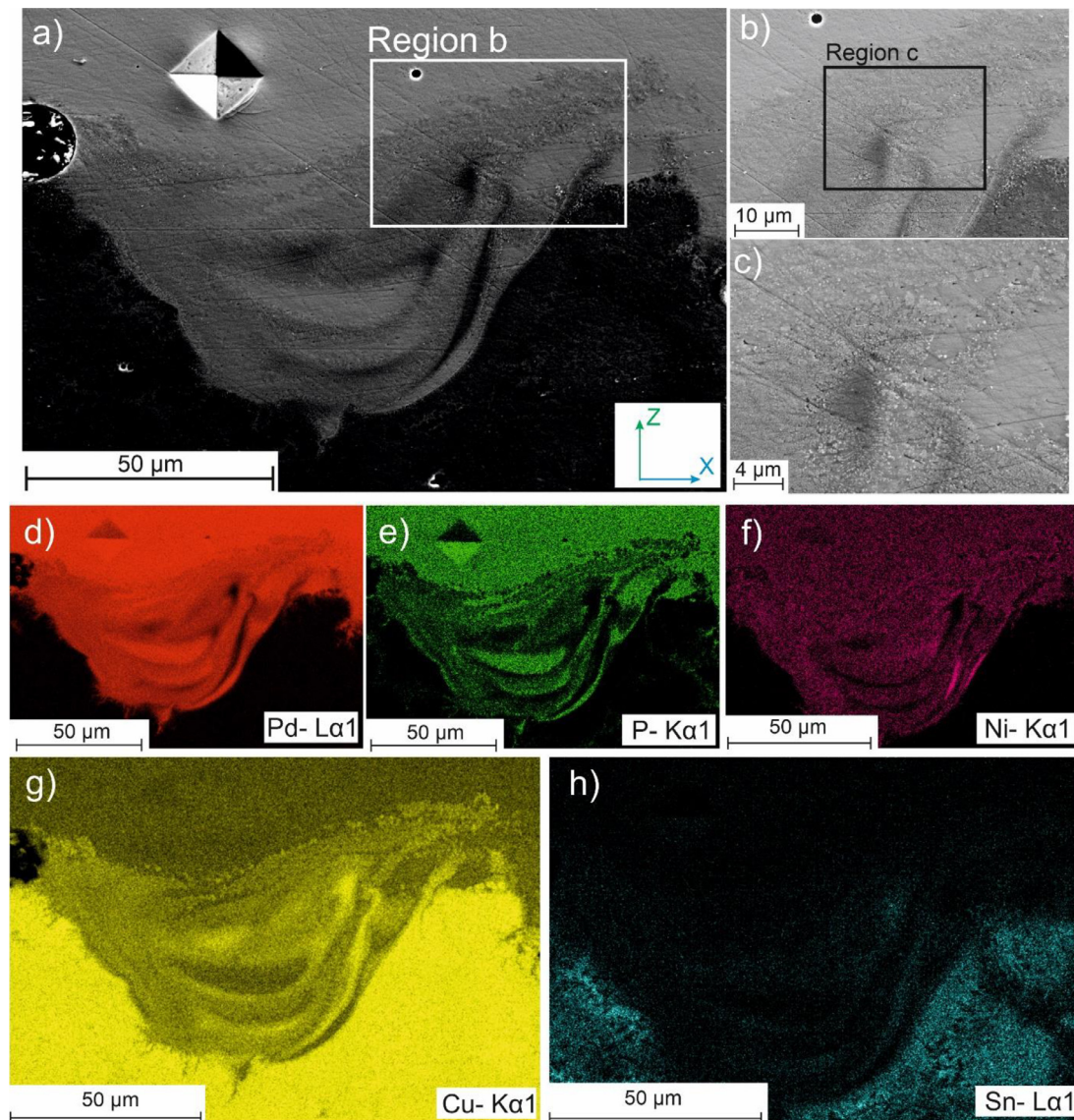


Fig. 10. (a) SEM image (BSE) at the interface between the Pd-based BMG and the bronze substrate; (b) higher magnification of region b in a); (c) higher magnification of region c in b), which shows the presence of (nano-)crystals. (d-h) EDS maps (accelerating voltage of 20 kV), revealing the distribution of Pd, P, Ni, Cu, and Sn, respectively.

Table 2

EDS results in at% (average value and standard deviation of 12 measurements) for the powder and the LPBF-processed sample at different locations (see Fig. 13b), using an accelerating voltage of 30 kV.

Sample	Location	Pd	Cu	Ni	P	Al	Si	Fe	Cr
Nominal Powder	–	43	27	10	20	–	–	–	–
LPBF sample	Cross-section	40.4 ± 0.4	30.1 ± 0.6	11.1 ± 0.3	16.8 ± 1.0	1.0 ± 0.1	0.6 ± 0.1	0	0
	Amorphous matrix	40.4 ± 0.2	29.7 ± 0.3	10.9 ± 0.1	17.3 ± 0.1	0.9 ± 0.1	0.6 ± 0.0	0.1 ± 0.1	0.1 ± 0.1
	White nanocrystals	39.9 ± 0.5	33.6 ± 2.2	10.4 ± 1.1	13.9 ± 1.0	1.2 ± 0.1	0.6 ± 0.1	0.3 ± 0.1	0.1 ± 0.1
	Dark nanocrystals	33.0 ± 3.6	23.6 ± 2.6	12.9 ± 1.5	18.6 ± 2.2	0.8 ± 0.1	0.6 ± 0.1	7.4 ± 2.3	3.1 ± 1.2

tallization. Fig. 12a shows the eight diffraction patterns collected at different points as illustrated in the inset. The beam spot on the sample was fixed to 0.4 mm × 0.4 mm, while the center-to-center distance from one spot to the next was 0.6 mm.

Only the diffraction pattern corresponding to the sampling point P5 in Fig. 12 reveals a diffraction profile free from any crystalline feature. All other diffraction patterns show, in addition to two humps related the amorphous part of the sample, a series of small crystalline peaks. Their weak intensity suggests that they originate from one or more crystalline phases with a very low vol-

ume fraction compared to that of the amorphous matrix, and refer to a cubic phase Pm-3 m with $a = 2.987 \text{ \AA}$. This is in agreement with the crystallographic information obtained for the CuPd (ratio 1:1) phase (181,913-ICSD, [90]) and a few additional unidentified phase/s. To further investigate these crystals, the sample was polished up to a colloidal silica solution with a particle size of 50 nm, and was then studied by SEM in back-scattered electron (BSE) mode.

Fig. 13a,b shows BSE images of the polished sample. Dark and white crystals are easily detectable. Fig. 13b shows a higher mag-

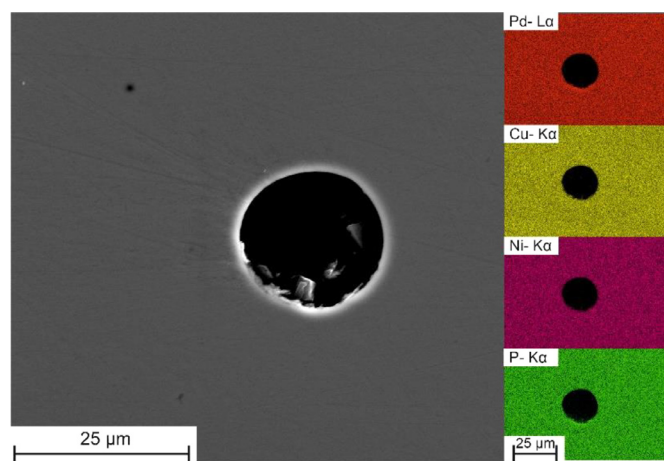


Fig. 11. EDS analysis (accelerating voltage of 30 kV) around a pore to determine the distribution of Pd, Cu, Ni and P. The insets show the elemental maps.

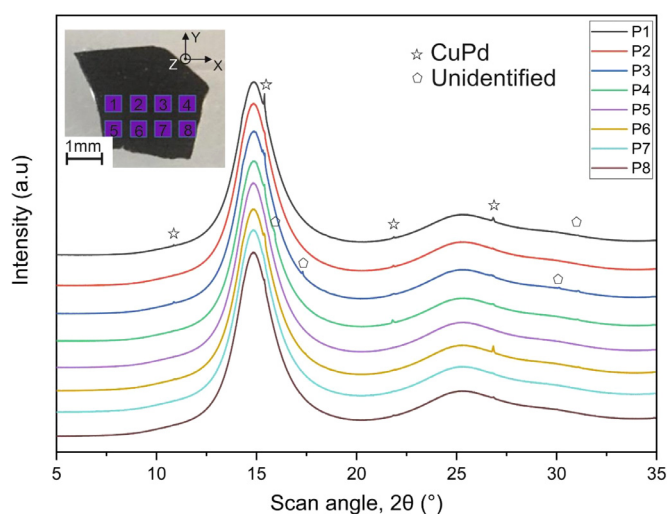


Fig. 12. Diffraction patterns of eight different locations of sample 4 (see inset) measured with synchrotron X-ray radiation using a wavelength of 0.5638 Å.

nification of region b in Fig. 13a. The crystal size is in the nanometer range and always below 1 μm . EDS analysis (using an accelerating voltage of 30 kV and a beam current of 1.2 nA) was performed on the cross-sections of the powder, the amorphous matrix (area 1), and the nanocrystals (point 1 and point 2) in Fig. 13b, and the spectra are presented in Fig. 13c-f. Table 2 presents the average values and standard deviations of the EDS results of 12 measurements for the powder cross-section, amorphous matrix, and nanocrystals at different locations (only one of the locations is shown in Fig. 13b for the amorphous matrix and nanocrystals). Area 1 does not include any detectable features, and the chemical composition is close to the one of the powder. Point 1 is richer in Cu compared to the amorphous matrix and also appears brighter, which means that it has a higher atomic weight. These white nanocrystals may thus be attributed to the CuPd phase identified in the diffraction patterns (see Fig. 12). The chemical compositions of area 1 and point 1 reveal the presence of Fe and Cr in the LPBF sample, which are not present in the powder. The measured composition of the nanocrystals embedded in the amorphous matrix is different from those of the crystals isothermally formed at 317 $^{\circ}\text{C}$ by Wanderka et al. [91] and at 427 $^{\circ}\text{C}$, and 382 $^{\circ}\text{C}$ by Löf-ler et al. [19] in a $\text{Pd}_{40}\text{Cu}_{30}\text{Ni}_{10}\text{P}_{20}$ alloy; at 450 $^{\circ}\text{C}$ by Jaeger et al. [92] in a $\text{Pd}_{43}\text{Cu}_{27}\text{Ni}_{10}\text{P}_{20}$ alloy; and at 497 $^{\circ}\text{C}$ by Ma et al. [93] for

PdCuNiP glass-forming alloys of different composition. However, it should be noted that the interaction volume of electrons during EDS measurements at 30 kV may be larger than the crystal volume, so that the measured crystal composition may deviate from the actual value. The presence of Al and Si may come from the impurities in the powder feedstock or from the grinding and polishing processes; and Fe and Cr are attributed to residual impurities in the LPBF machine. The CuPd phase nanocrystals (white nanocrystals, point 1 in Fig. 13b) formed adjacent to the dark nanocrystals seen in Fig. 13b (point 2), which indicates that the formation of the CuPd nanocrystals was triggered by the presence of impurities. A change in the chemical composition of BMGs often generates crystallization [44,94], which was also seen in the first printed layer (Fig. 10) as a result of an intermixing with the substrate.

3.5. Crystallization kinetics of the powder used in the LPBF process

The crystallization kinetics of bulk $\text{Pd}_{43}\text{Cu}_{27}\text{Ni}_{10}\text{P}_{20}$ have been studied intensively [18,91,95–98]. Here, we studied the crystallization of individual powder particles, because understanding of their crystallization kinetics is critical to generate a fully amorphous structure in the LPBF process. To obtain a TTT diagram, we melted the powder alloy at 600 $^{\circ}\text{C}$ in the FDSC 2+ device, undercooled the melt at a rate of 1000 K/s to different temperatures between 350 and 500 $^{\circ}\text{C}$, and held it isothermally for 1000s. Twelve measurements were performed for each isothermal temperature. Fig. 14a shows isothermal FDSC curves for temperatures between 380 and 460 $^{\circ}\text{C}$. The times of the start and end of crystallization are indicated by arrows for each temperature. After isothermal hold, the sample was cooled to 50 $^{\circ}\text{C}$ and heated again to 600 $^{\circ}\text{C}$ with a rate of 1000 K/s to melt the material for the next isothermal measurement. The presence of complete, partial, or no crystallization during the isothermal hold was confirmed by the subsequent heating curves (Fig. 14b). In the case where no crystallization occurred during isothermal hold, only the glass transition but no melting was observed during the subsequent heating scan at a rate of 1000 K/s (black curve). In the case of complete crystallization, no glass transition but only melting was seen upon heating (red curve). A glass transition and a melting event were observed when the sample had crystallized partially during the previous isothermal hold (blue curve), but no exothermic crystallization was detected before melting.

The critical cooling rate for glass formation was measured as 0.1 to 0.5 K/s before and after all isothermal measurements, which shows that the crystallization kinetics did not change as a result of any potential reaction between the sample and the FDSC sensor. The range of critical cooling rates is very close to those reported by Schroers et al. [99], which are 0.4 K/s for the untreated alloy and 0.09 K/s after B_2O_3 fluxing.

The critical heating rate has not been evaluated in detail, but it can be concluded from Fig. 14b that it is significantly less than 1000 K/s, because no (further) crystallization has been observed for amorphous or partially crystalline samples upon heating at 1000 K/s (see black and blue curves in Fig. 14b). Preliminary experiments reveal that the critical heating rate of the PdCuNiP powder is indeed 10 K/s or less. In our previous study on LPBF of a Zr-based BMG [61], using FEM simulation we showed that the related heating and cooling rates in the HAZ are in the order of 10^6 K/s, i.e. much higher than the alloy's critical heating and cooling rates, which were measured as 45,000 K/s and 2500 K/s, respectively [75]. Since crystallization was nevertheless detected in the HAZ, we conclude that the time spent at high temperatures is the reason for crystallization. Other studies on LPBF of BMGs also confirmed that the heating rate in the HAZ is higher than 10^5 K/s (see Refs. [35,36,56]).

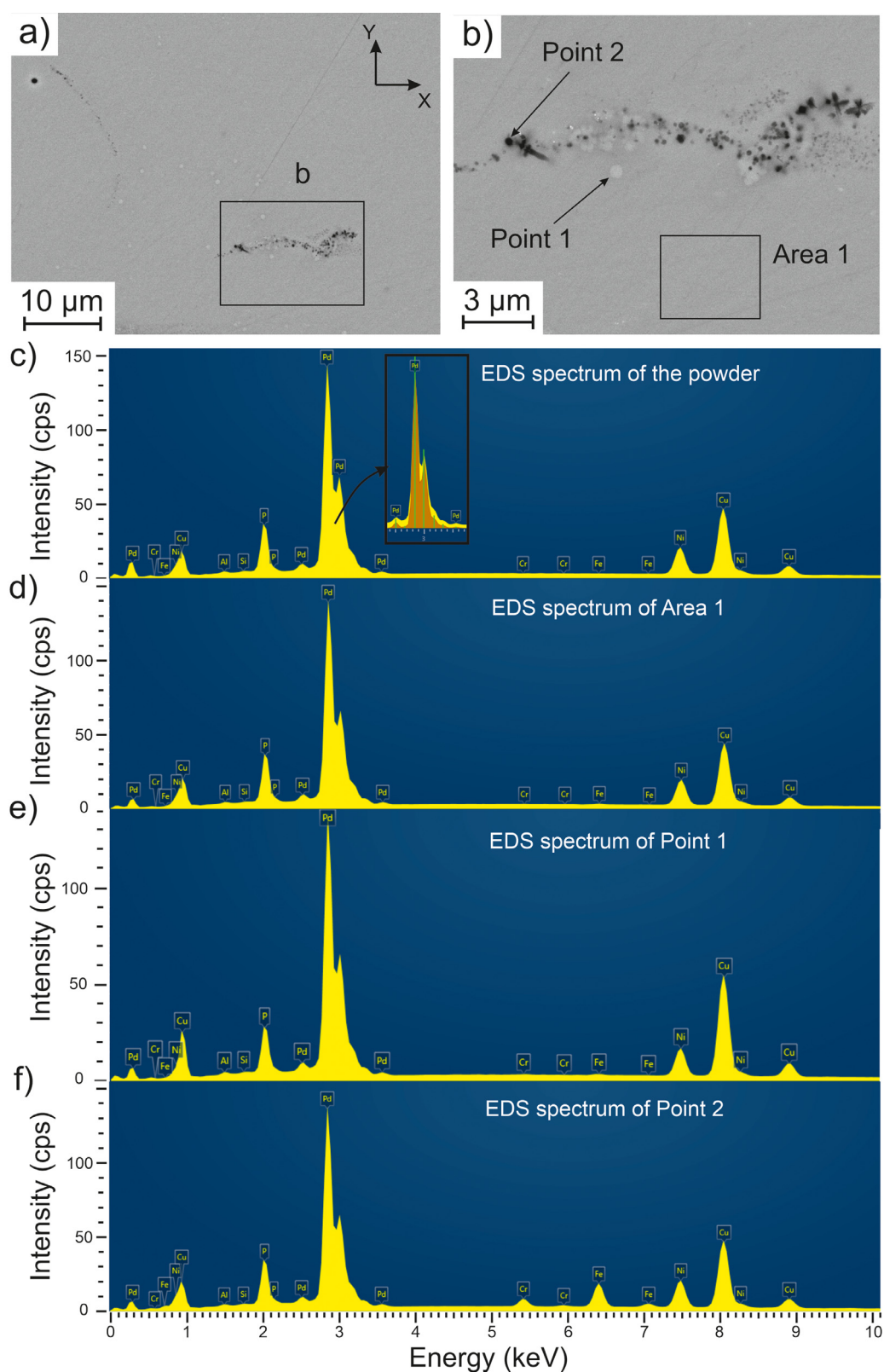


Fig. 13. (a) BSE image of sample 4, revealing the presence of nanocrystals embedded in the amorphous matrix. (b) Higher magnification of region b in a). EDS spectra (using 30 kV accelerating voltage and 1.2 nA beam current) of (c) the powder cross-section, (d) area 1 shown in b), and (e,f) points 1 and 2 shown in b). The horizontal axis of the EDS spectra indicates the accelerating energy (in keV).

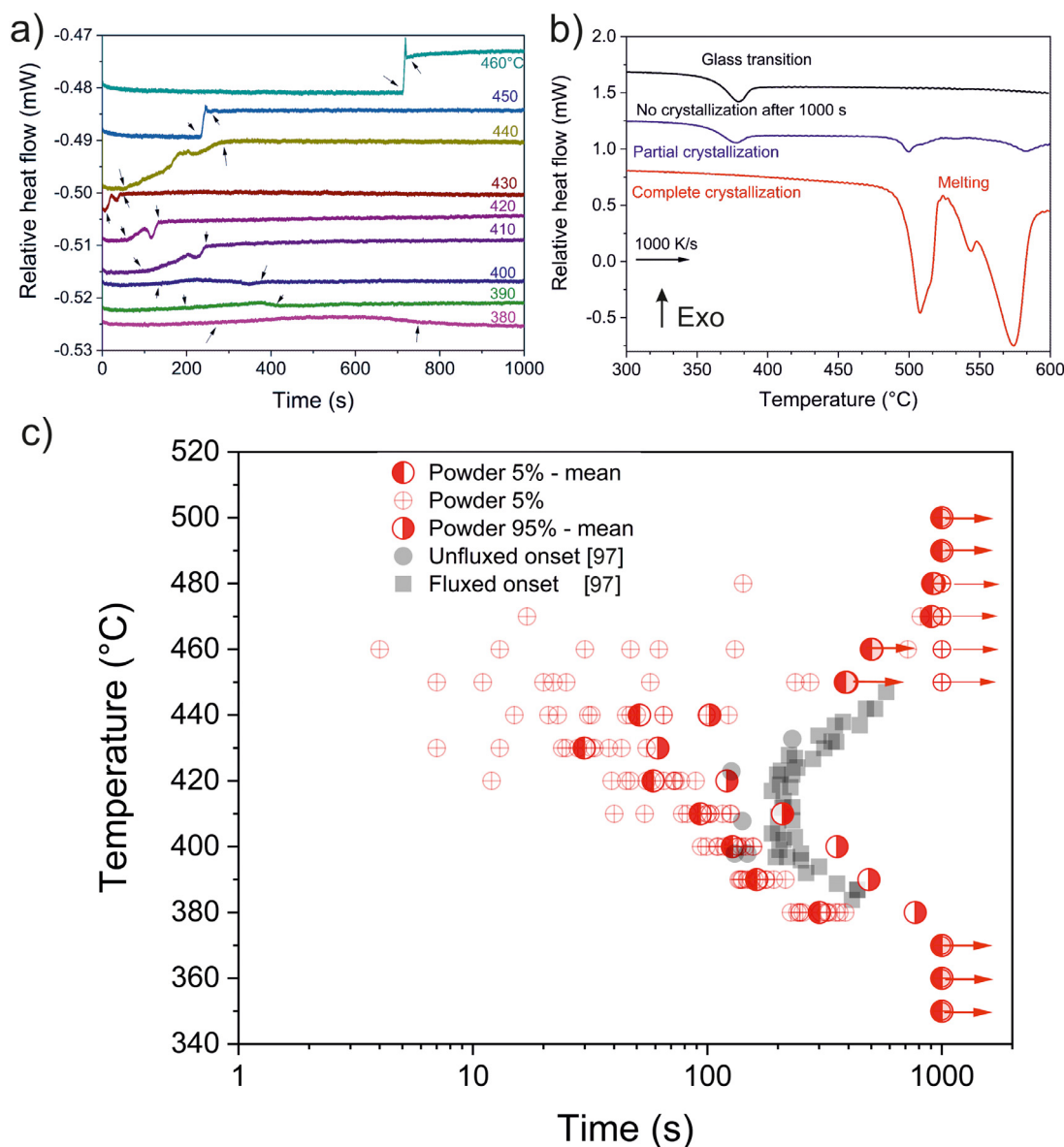


Fig. 14. (a) Isothermal FDSC curves of $\text{Pd}_{43}\text{Cu}_{27}\text{Ni}_{10}\text{P}_{20}$ powder at temperatures between 380 and 460 °C for 1000s of isothermal hold after the liquid was cooled from 600 °C with a rate of 1000 K/s. The arrows indicate the start and end of crystallization for each temperature. (b) FDSC heating curves at a rate of 1000 K/s, showing no, partial or complete crystallization during the previous isothermal hold for 1000s in the undercooled liquid range. (c) Time-Temperature-Transformation (TTT) diagram showing the crystallization kinetics of a single powder with a mass of 0.4 μg . While half-filled circles indicate the mean crystallization times of 12 measurements to obtain 5% and 95% crystallization, the open circles with centerlines demonstrate the individual values for 5% crystallization. At temperatures above 440 °C and below 380 °C, crystallization could not be observed even after 1000s for some or all of the isothermal measurements. These measurements were, however, still taken into account in the calculation of the mean values by assuming a crystallization time of 1000s. In this case, red arrows are used to demonstrate that the actual or mean crystallization times are larger than those given. The crystallization onset times of the untreated (filled circles) and B_2O_3 -fluxed (filled squares) bulk samples of about 200 mg, taken from Ref. [96], are also presented for comparison.

Fig. 14c shows a TTT diagram for the $\text{Pd}_{43}\text{Cu}_{27}\text{Ni}_{10}\text{P}_{20}$ powder alloy, which was obtained by repeated melting and crystallization of a single FDSC sample with a mass of 0.4 μg . In the temperature ranges of 350–370 °C and 450–500 °C no crystallization was observed during 1000s of isothermal hold for some or all of the measurements.

The time scales for 5% and 95% crystallization were determined from the total heat released during isothermal crystallization. The individual values for 5% crystallization are shown in the TTT diagram by open circles with center lines, and the corresponding mean crystallization values by half-filled circles (left-filled circles: 5%, right-filled circles: 95% of crystallization). The measurements where crystallization was not observed after 1000s were still taken into account in the calculation of the mean values by assuming

a crystallization time of 1000s. However, arrows indicating larger time scales were used to demonstrate that the actual values are higher than the given ones. For comparison, the crystallization onset times reported by Schroers et al. [96] are also presented in Fig. 14c by gray symbols. Although the measured critical cooling rates for glass formation are comparable with those reported in [96], the crystallization times for the powder alloy are significantly different. While nucleation is less probable in the FDSC powder samples, which are half a million times smaller than the bulk samples, the powder alloy still crystallizes faster than the bulk alloy, probably due to the contamination of the powder with Al and Si during the atomization process (Fig. 13c, Table 2). While the crystallization times at the nose of the TTT diagram for the bulk samples are higher than 100 s between 400 and 430 °C [96,99], the

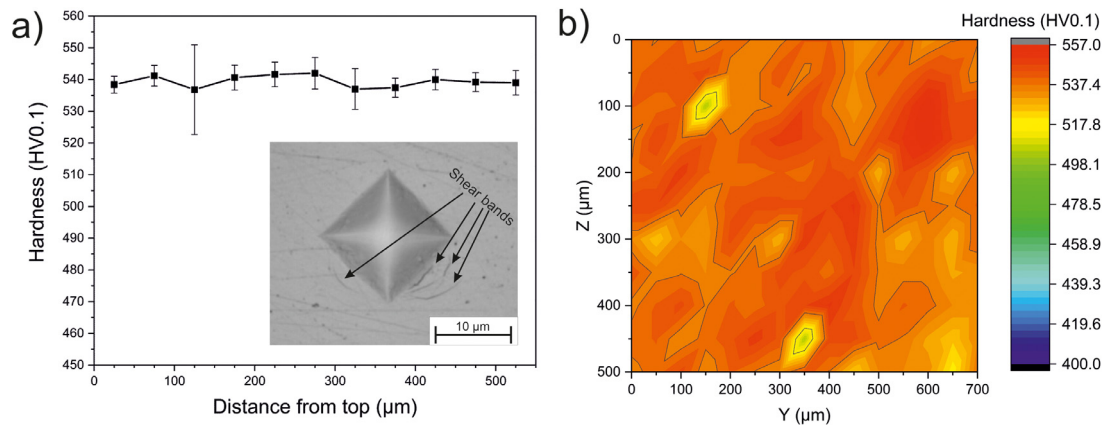


Fig. 15. (a) Microhardness results (HV0.1) from the top surface until 525 μm below the surface; the inset illustrates shear band propagation caused by an indentation. The large error at around 100 μm below the melt pool probably results from the presence of nanocrystals or defects below the surface. (b) Hardness map obtained with 165 indentations.

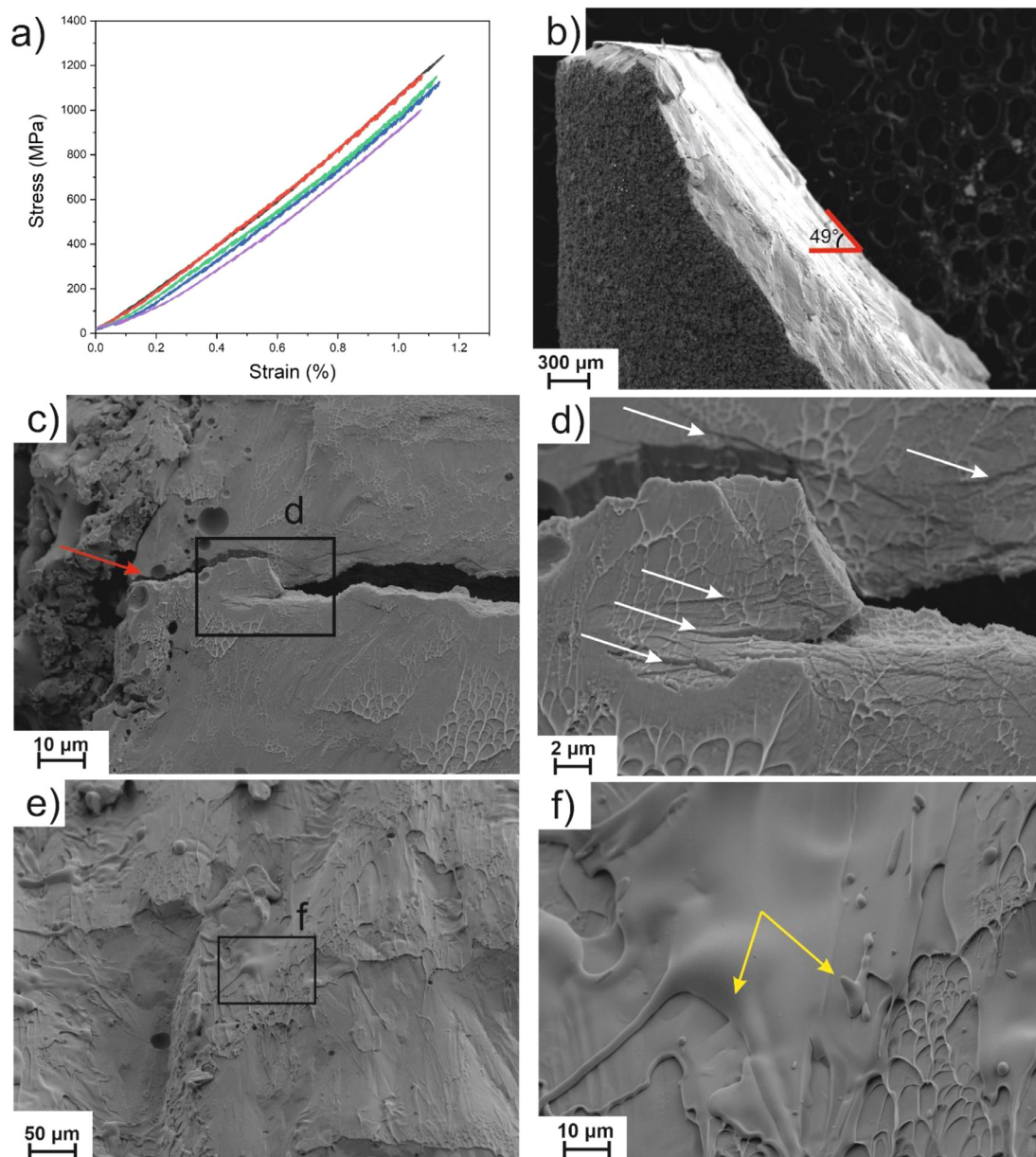


Fig. 16. (a) Compressive stress-strain curves of five LPBF-processed PdCuNiP samples. (b) Macroscopic SEM image (secondary electron, SE) of the cylindrical specimen after failure in a uniaxial compression test. (c) Micrograph of a crack initiated from the surface of the cylinder, with the red arrow illustrating crack propagation through a pore. (d) Magnified region d, illustrated in c), revealing shear bands (see white arrows). (e) Micrograph from another location of the fracture surface. (f) Magnified region f, illustrated in e), showing liquid-like features (yellow arrows).

mean crystallization time (5%) is about 30 s at 430 °C for the powder alloy. As has also been observed in Ref. [100], the crystallization times scatter significantly not only for the temperature range where crystallization is mainly controlled by nucleation (at and above 450 °C), but also for the temperature range near the nose of the TTT diagram where crystallization is controlled by both nucleation and growth (410–440 °C). No dependence of crystallization time on measurement number was observed, which excludes any “history effect”.

The minimum crystallization time (5%) was measured as 4 s at 460 °C. While this value is two orders of magnitude smaller than the mean value, it is still much larger than the LPBF processing time, which is less than 100 ms. The FDSC measurements therefore cannot explain the formation of nanocrystals, as observed in Fig. 13a–b. However, it should be noted that while the powder alloy does not contain Fe and Cr, the nanocrystals embedded in the amorphous matrix of the LPBF-processed alloy contain a significant amount of such elements (Fig. 13e, Table 2). These elements may promote crystallization and thus deteriorate the glass-forming ability of the PdCuNiP alloy.

3.6. Mechanical properties

The hardness (HV1) of five indents on the X-Z cross-section of the optimized sample is 498.4 ± 4.2 , which is somewhat lower than the HV1 = 510 value reported for an amorphous as-cast sample with a slightly different chemical composition ($\text{Pd}_{40}\text{Cu}_{30}\text{Ni}_{10}\text{P}_{20}$) [101].

Fig. 15a presents the hardness values (HV0.1) from the top surface up to 525 μm below the surface for the optimized sample. A lower force of 100 g was used to investigate the hardness along the sample's depth and to plot a hardness map. The sample reveals almost uniform hardness throughout its thickness. The inset of Fig. 15a shows the propagation of shear bands due to local plastic deformation caused by an indentation. The hardness map (HV 0.1) is shown in Fig. 15b. The hardness in the tested area is relatively uniform, indicating a homogeneous structure. Two regions with greenish color have a lower hardness because the indenting was performed close to pores. The average hardness of 165 indentations is 539 ± 7 (HV0.1).

Five compression tests at a strain rate of $1 \times 10^{-4} \text{ s}^{-1}$ were carried out on the LPBF-processed samples and resulted in a fracture strength of $1138 \pm 78 \text{ MPa}$ (see Fig. 16a), which is lower than the reported 1326 MPa value of an as-cast Pd-based BMG with a slightly different chemical composition [101]. The strain to failure was $1.17 \pm 0.08 \%$. Similar to Refs [61,101], no macroscopic plastic deformation was detected. Kumar et al. [102] also reported no plastic deformation and a strain to failure of less than 2% in bending of a $\text{Pd}_{43}\text{Cu}_{27}\text{Ni}_{10}\text{P}_{20}$ BMG having the same chemical composition as investigated in this study.

Fig. 16b shows the macroscopic image of the cylindrical sample after rupture. The fracture angle is inclined at around 49°, marginally different from the maximum shear-stress plane of 45°. A crack starting from the surface is shown in Fig. 16c, which propagates through the pores present in the sample (red arrow). The lower fracture strength of the LPBF sample compared to the as-cast sample [101] may be due to the presence of such defects (0.40 vol%). Vein-like patterns are visible in Fig. 16c and are attributed to significant softening or reduced viscosity during fracture [103]. Fig. 16d enlarges the region d illustrated in Fig. 16b. Shear bands close to the crack are indicated by white arrows, which according to Li et al. [104] probably initiated the catastrophic failure. Fig. 16e–f presents the formation of liquid-like features (yellow arrows in Fig. 16f), in addition to the vein-like patterns. Following Argon et al. [105] and Dalla Torre et al. [103], these indicate a significant temperature rise in the final stage of fracture due to the

instantaneous release of stored elastic energy, with local plasticity and softening.

All experiments in this study were performed using less than 70 g of Pd-based metallic glass powder, with a strategy that minimized time, material, and cost, which is of particular importance for precious metals.

4. Conclusion

In this study, a Pd-based $\text{Pd}_{43}\text{Cu}_{27}\text{Ni}_{10}\text{P}_{20}$ bulk metallic glass (BMG) manufactured via Laser Powder-Bed Fusion (LPBF) was characterized, looking in detail at the microstructure and mechanical properties of the bulk samples, and the crystallization kinetics of the amorphous powder particles. The outcome can be summarized as follows:

- 1) Processing parameters such as laser power and scanning speed were optimized from single laser-track experiments.
- 2) High Volume Energy Density (VED) leads to irregularities in the shape of the single tracks and of the final parts due to heat accumulation.
- 3) Using single-track optimized parameters, a highly amorphous sample was produced, with a density of 99.60%, measured by micro-computed tomography.
- 4) Studying the crystallization kinetics of the atomized powder generated a complete TTT diagram upon cooling, which reveals that the time scales for crystallization ($>4 \text{ s}$) are far above the processing time ($<100 \text{ ms}$) in the LPBF process. The powder crystallization may thus result from Al and Si contamination during the atomization process.
- 5) Despite the good glass-forming ability (GFA) of Pd-based BMG, the critical aspects in LPBF fabrication for avoiding crystallization are not so much the thermal conditions related to laser parameters, but more the absence of impurities during the LPBF process.
- 6) Excellent mechanical properties such as high hardness and compressive strength were achieved despite the presence of some porosity and nanocrystals. The compressive strength is only 14% lower than the value reported for an as-cast Pd-based BMG with similar chemical composition.
- 7) The present work illustrates how the combination of precious metals, amorphous state, and additive manufacturing can lead to promising applications, especially in the jewelry and watch industries.

Declaration of Competing Interest

None.

CRediT authorship contribution statement

Navid Sohrabi: Conceptualization, Methodology, Formal analysis, Investigation, Writing – original draft, Visualization. **Jamasap Jhabvala:** Conceptualization, Supervision, Validation, Writing – review & editing. **Güven Kurtuldu:** Methodology, Validation, Formal analysis, Investigation, Writing – original draft. **Ruggero Frison:** Methodology, Formal analysis, Writing – review & editing. **Annapaola Parrilli:** Methodology, Formal analysis, Writing – review & editing. **Mihai Stoica:** Resources, Supervision, Validation, Methodology, Formal analysis, Writing – review & editing. **Antonia Neels:** Resources, Writing – review & editing. **Jörg F. Löffler:** Conceptualization, Resources, Supervision, Validation, Writing – review & editing. **Roland E. Logé:** Conceptualization, Resources, Supervision, Validation, Project administration, Funding acquisition, Writing – review & editing.

Data availability

The raw data required to reproduce these findings are available to download from [<https://drive.google.com/drive/folders/1OvxjPOOA9jpFDkDKdh3YXiv1uVgEMGiQ?usp=sharing>]. The processed data required to reproduce these findings are available to download from [<https://drive.google.com/drive/folders/1NGSxJ6pV02vpFK8FJHVAu5ZOflxIOI4?usp=sharing>].

Acknowledgment

This work was supported by the “PREcision Additive Manufacturing of Precious metals Alloys (PREAMPA)” project, funded by the Swiss ETH domain within the Strategic Focus Area on Advanced Manufacturing. The generous support of PX Group to the LMTM laboratory is also gratefully acknowledged.

References

- [1] H. Heidsiek, M. Casing, The abrasive wear of gold jewellery alloys, *Gold Bull.* 16 (1983) 76–81, doi:[10.1007/BF03214627](https://doi.org/10.1007/BF03214627).
- [2] R. Süß, E. Van Der Lingen, L. Glaner, M.Du Toit, 18 Carat Yellow Gold Alloys With Increased Hardness, *Gold Bull.* 37 (2004) 196–207, doi:[10.1007/BF03215213](https://doi.org/10.1007/BF03215213).
- [3] J. Schroers, B. Lohwongwatana, W.L. Johnson, A. Peker, Gold based bulk metallic glass, *Appl. Phys. Lett.* 87 (2005) 1–4, doi:[10.1063/1.2008374](https://doi.org/10.1063/1.2008374).
- [4] S. Cardinal, J.M. Pelletier, M. Eisenbart, U.E. Klotz, Influence of crystallinity on thermo-process ability and mechanical properties in a Au-based bulk metallic glass, *Mater. Sci. Eng. A.* 660 (2016) 158–165, doi:[10.1016/j.msea.2016.02.078](https://doi.org/10.1016/j.msea.2016.02.078).
- [5] H.G. Schenzel, T. Laag, Precious metal alloy for use in the jewelry and watch industry, US10119177B2, 2018. <https://patentimages.storage.googleapis.com/de/de/14/a0d7490170c49a/US10119177.pdf>.
- [6] T. Biggs, S.S. Taylor, E. Van Der Lingen, The hardening of platinum alloys for potential jewellery application, *Platin. Met. Rev.* 49 (2005) 2–15, doi:[10.1595/147106705X24409](https://doi.org/10.1595/147106705X24409).
- [7] R. Süß, E. Van Der Lingen, L. Glaner, M.Du Toit, 18 carat yellow gold alloys with increased hardness, *Gold Bull.* 37 (2004) 196–207, doi:[10.1007/BF03215213](https://doi.org/10.1007/BF03215213).
- [8] J. Brelle, A. Blatter, R. Ziegenhagen, Precious palladium-aluminium-based alloys with high hardness and workability, *Platin. Met. Rev.* 53 (2009) 189–197, doi:[10.1595/147106709X472192](https://doi.org/10.1595/147106709X472192).
- [9] G.H. Jeon, Y.H. Kwon, H.J. Seol, H. Il Kim, Hardening and overaging mechanisms in an Au-Ag-Cu-Pd alloy with in additions, *Gold Bull.* 41 (2008) 257–263, doi:[10.1007/BF03214879](https://doi.org/10.1007/BF03214879).
- [10] J.F. Löffler, A.A. Kündig, F.H. Dalla Torre, *Rapid Solidification and Bulk Metallic Glasses – Processing and Properties*, in: *Mater. Process. Handb.*, Taylor & Francis Group, New York, 2007.
- [11] W. Klement, R.H. Willens, P.O.L. Duwez, Non-crystalline Structure in Solidified Gold-Silicon Alloys, *Nature* 187 (1960) 869–870, doi:[10.1038/187869b0](https://doi.org/10.1038/187869b0).
- [12] N. Nishiyama, A. Inoue, Glass-forming ability of bulk Pd₄₀Ni₁₀Cu₃₀P₂₀ alloy, *Mater. Trans. JIM.* 37 (1996) 1531–1539, doi:[10.2320/matertrans1989.37.1531](https://doi.org/10.2320/matertrans1989.37.1531).
- [13] H. Kazemi, C. Cattin, M. Blank, L. Weber, Development of a new family of phosphorous-free Pt-based bulk metallic glasses, *J. Alloys Compd.* 695 (2017) 3419–3428, doi:[10.1016/j.jallcom.2016.12.017](https://doi.org/10.1016/j.jallcom.2016.12.017).
- [14] K.J. Laws, K.F. Shamlaye, M. Ferry, Synthesis of Ag-based bulk metallic glass in the Ag-Mg-Ca-[Cu] alloy system, *J. Alloys Compd.* 513 (2012) 10–13, doi:[10.1016/j.jallcom.2011.10.097](https://doi.org/10.1016/j.jallcom.2011.10.097).
- [15] H.W. Kui, A.L. Greer, D. Turnbull, Formation of bulk metallic glass by fluxing, *Appl. Phys. Lett.* 45 (1984) 615–616, doi:[10.1063/1.95330](https://doi.org/10.1063/1.95330).
- [16] D. Granata, E. Fischer, V. Wessels, J.F. Löffler, The detrimental effect of flux-induced boron alloying in Pd-Si-Cu bulk metallic glasses, *Appl. Phys. Lett.* 106 (2015) 11902, doi:[10.1063/1.4905174](https://doi.org/10.1063/1.4905174).
- [17] A. Inoue, N. Nishiyama, H. Kimura, Preparation and thermal stability of Bulk Amorphous Pd₄₀Cu₃₀Ni₁₀P₂₀ alloy cylinder of 72mm in diameter, *Mater. Trans.* 38 (1997) 179–183, doi:[10.1016/S0022-3093\(03\)00006-1](https://doi.org/10.1016/S0022-3093(03)00006-1).
- [18] I. Lu, G. Wilde, G.P. Görlner, R. Willnecker, *Thermodynamic properties of Pd-based glass-forming alloys*, *J. Non. Cryst. Solids.* 252 (1999) 577–581.
- [19] J.F. Löffler, J. Schroers, W.L. Johnson, Time-temperature-transformation diagram and microstructures of bulk glass forming Pd₄₀Cu₃₀Ni₁₀P₂₀, *Appl. Phys. Lett.* 77 (2000) 681–683, doi:[10.1063/1.127084](https://doi.org/10.1063/1.127084).
- [20] S. Pauly, L. Löber, R. Petters, M. Stoica, S. Scudino, U. Kühn, J. Eckert, Processing metallic glasses by selective laser melting, 2013. doi:[10.1016/j.mattod.2013.01.018](https://doi.org/10.1016/j.mattod.2013.01.018).
- [21] J. Schroers, Processing of Bulk Metallic Glass, *Adv. Mater.* 22 (2010) 1566–1597, doi:[10.1002/adma.200902776](https://doi.org/10.1002/adma.200902776).
- [22] Z. Mahbooba, L. Thorsson, M. Unosson, P. Skoglund, H. West, T. Horn, C. Rock, E. Vogli, O. Harrysson, Additive manufacturing of an iron-based bulk metallic glass larger than the critical casting thickness, *Appl. Mater. Today.* 11 (2018) 264–269, doi:[10.1016/j.apmt.2018.02.011](https://doi.org/10.1016/j.apmt.2018.02.011).
- [23] S. Cardinal, J.M. Pelletier, M. Eisenbart, U.E. Klotz, Influence of crystallinity on thermo-process ability and mechanical properties in a Au-based bulk metallic glass, *Mater. Sci. Eng. A.* 660 (2016) 158–165, doi:[10.1016/j.msea.2016.02.078](https://doi.org/10.1016/j.msea.2016.02.078).
- [24] S. Cardinal, J. Qiao, J.M. Pelletier, H. Kato, Bulk metallic glasses based on precious metals: thermal treatments and mechanical properties, *Intermetallics* 63 (2015) 73–79, doi:[10.1016/j.intermet.2015.04.003](https://doi.org/10.1016/j.intermet.2015.04.003).
- [25] S. Gravier, G. Kapelski, M. Suéry, J.J. Blandin, Thermoplastic forming of bulk metallic glasses, *Int. J. Appl. Glas. Sci.* 3 (2012) 180–187, doi:[10.1111/j.2041-1294.2012.00083.x](https://doi.org/10.1111/j.2041-1294.2012.00083.x).
- [26] T. DeRoy, H.L. Wei, J.S. Zuback, T. Mukherjee, J.W. Elmer, J.O. Milewski, A.M. Beese, A. Wilson-Heid, A. De, W. Zhang, Additive manufacturing of metallic components – Process, structure and properties, *Prog. Mater. Sci.* 92 (2018) 112–224, doi:[10.1016/j.pmatsci.2017.10.001](https://doi.org/10.1016/j.pmatsci.2017.10.001).
- [27] D.D. Gu, W. Meiners, K. Wissenbach, R. Poprawe, Laser additive manufacturing of metallic components: materials, processes and mechanisms, *Int. Mater. Rev.* 57 (2012) 133–164, doi:[10.1179/1743280411Y.00000000014](https://doi.org/10.1179/1743280411Y.00000000014).
- [28] T. Vilaro, V. Kottman-Rexerodt, M. Thomas, C. Colin, P. Bertrand, L. Thivillon, S. Abed, V. Ji, P. Aubry, P. Peyre, T. Malot, in: *Direct Fabrication of a Ti-47Al-2Cr-2Nb Alloy By Selective Laser Melting and Direct Metal Deposition Processes*, in: *THERMEC 2009 Suppl.*, Trans Tech Publications, 2010, pp. 586–591, doi:[10.4028/www.scientific.net/AMR.89-91.586](https://doi.org/10.4028/www.scientific.net/AMR.89-91.586).
- [29] S. Katakam, J.Y. Hwang, S. Paital, R. Banerjee, H. Vora, N.B. Dahotre, In Situ Laser Synthesis of Fe-Based Amorphous Matrix Composite Coating on Structural Steel, *Metall. Mater. Trans. A.* 43 (2012) 4957–4966, doi:[10.1007/s11661-012-1312-4](https://doi.org/10.1007/s11661-012-1312-4).
- [30] B. Zheng, Y. Zhou, J.E. Smugeresky, E.J. Lavernia, Processing and Behavior of Fe-Based Metallic Glass Components via Laser-Engineered Net Shaping, *Metall. Mater. Trans. A.* 40 (2009) 1235–1245, doi:[10.1007/s11661-009-9828-y](https://doi.org/10.1007/s11661-009-9828-y).
- [31] S.X. Liang, X. Wang, W. Zhang, Y.J. Liu, W. Wang, L.C. Zhang, Selective laser melting manufactured porous Fe-based metallic glass matrix composite with remarkable catalytic activity and reusability, *Appl. Mater. Today.* 19 (2020) 100543, doi:[10.1016/j.apmt.2019.100543](https://doi.org/10.1016/j.apmt.2019.100543).
- [32] X.D. Nong, X.L. Zhou, Y.X. Ren, Fabrication and characterization of Fe-based metallic glasses by Selective Laser Melting, *Opt. Laser Technol.* 109 (2019) 20–26, doi:[10.1016/j.optlastec.2018.07.059](https://doi.org/10.1016/j.optlastec.2018.07.059).
- [33] N. Li, J. Zhang, W. Xing, D. Ouyang, L. Liu, 3D printing of Fe-based bulk metallic glass composites with combined high strength and fracture toughness, *Mater. Des.* 143 (2018) 285–296, doi:[10.1016/j.matdes.2018.01.061](https://doi.org/10.1016/j.matdes.2018.01.061).
- [34] H.Y. Jung, S.J. Choi, K.G. Prashanth, M. Stoica, S. Scudino, S. Yi, U. Kühn, D.H. Kim, K.B. Kim, J. Eckert, Fabrication of Fe-based bulk metallic glass by selective laser melting: a parameter study, *Mater. Des.* 86 (2015) 703–708, doi:[10.1016/j.matdes.2015.07.145](https://doi.org/10.1016/j.matdes.2015.07.145).
- [35] D. Ouyang, W. Xing, N. Li, Y. Li, L. Liu, Structural evolutions in 3D-printed Fe-based metallic glass fabricated by selective laser melting, *Addit. Manuf.* 23 (2018) 246–252, doi:[10.1016/j.addma.2018.08.020](https://doi.org/10.1016/j.addma.2018.08.020).
- [36] L. Wang, H. Wang, Y. Liu, Z. Fu, T. Peng, J. Shen, S. Zhou, M. Yan, G. Wang, Y. Dai, Selective laser melting helps fabricate record-large bulk metallic glass: experiments, simulation and demonstrative part, *J. Alloys Compd.* 808 (2019) 151731, doi:[10.1016/j.jallcom.2019.151731](https://doi.org/10.1016/j.jallcom.2019.151731).
- [37] D.C. Hofmann, P. Bordeenithikasem, A. Pate, S.N. Roberts, E. Vogli, Developing Processing Parameters and Characterizing Microstructure and Properties of an Additively Manufactured FeCrMoBc Metallic Glass Forming Alloy, *Adv. Eng. Mater.* (2018) 20, doi:[10.1002/adem.201800433](https://doi.org/10.1002/adem.201800433).
- [38] Y.G. Nam, B. Koo, M.S. Chang, S. Yang, J. Yu, Y.H. Park, J.W. Jeong, Selective laser melting vitrification of amorphous soft magnetic alloys with help of double-scanning-induced compositional homogeneity, *Mater. Lett.* 261 (2020) 127068, doi:[10.1016/j.matlet.2019.127068](https://doi.org/10.1016/j.matlet.2019.127068).
- [39] Y.M. Zou, Y.S. Wu, K.F. Li, C.L. Tan, Z.G. Qiu, D.C. Zeng, Selective laser melting of crack-free Fe-based bulk metallic glass via chessboard scanning strategy, *Mater. Lett.* 272 (2020) 2–5, doi:[10.1016/j.matlet.2020.127824](https://doi.org/10.1016/j.matlet.2020.127824).
- [40] K.G. Prashanth, H. Shakur Shahabi, H. Attar, V.C. Srivastava, N. Ellendt, V. Uhlenwinkel, J. Eckert, S. Scudino, Production of high strength Al₈₅Nd₅Ni₅Co₂ alloy by selective laser melting, *Addit. Manuf.* 6 (2015) 1–5, doi:[10.1016/j.addma.2015.01.001](https://doi.org/10.1016/j.addma.2015.01.001).
- [41] X.P. Li, M. Roberts, Y.J. Liu, C.W. Kang, H. Huang, T.B. Sercombe, Effect of substrate temperature on the interface bond between support and substrate during selective laser melting of Al-Ni-Y-Co-La metallic glass, *Mater. Des.* 65 (2015) 1–6, doi:[10.1016/j.matdes.2014.08.065](https://doi.org/10.1016/j.matdes.2014.08.065).
- [42] X.P. Li, C.W. Kang, H. Huang, L.C. Zhang, T.B. Sercombe, Selective laser melting of an Al₈₅Ni₅Y_{4.5}Co₂La_{1.5} metallic glass: processing, microstructure evolution and mechanical properties, *Mater. Sci. Eng. A.* 606 (2014) 370–379, doi:[10.1016/j.msea.2014.03.097](https://doi.org/10.1016/j.msea.2014.03.097).
- [43] X.P. Li, C.W. Kang, H. Huang, T.B. Sercombe, The role of a low-energy-density re-scan in fabricating crack-free Al₈₅Ni₅Y₆Co₂Fe₂ bulk metallic glass composites via selective laser melting, *Mater. Des.* 63 (2014) 407–411, doi:[10.1016/j.matdes.2014.06.022](https://doi.org/10.1016/j.matdes.2014.06.022).
- [44] X.P. Li, M.P. Roberts, S. O’Keeffe, T.B. Sercombe, Selective laser melting of Zr-based bulk metallic glasses: processing, microstructure and mechanical properties, *Mater. Des.* 112 (2016) 217–226, doi:[10.1016/j.matdes.2016.09.071](https://doi.org/10.1016/j.matdes.2016.09.071).
- [45] P. Bordeenithikasem, M. Stolpe, A. Elsen, D.C. Hofmann, Glass forming ability, flexural strength, and wear properties of additively manufactured Zr-based bulk metallic glasses produced through laser powder bed fusion, *Addit. Manuf.* 21 (2018) 312–317, doi:[10.1016/j.addma.2018.03.023](https://doi.org/10.1016/j.addma.2018.03.023).
- [46] P. Zhang, D. Ouyang, L. Liu, Enhanced mechanical properties of 3D printed Zr-based BMG composite reinforced with Ta precipitates, *J. Alloys Compd.* 803 (2019) 476–483, doi:[10.1016/j.jallcom.2019.06.303](https://doi.org/10.1016/j.jallcom.2019.06.303).

- [47] C. Zhang, X. min Li, S.Q. Liu, H. Liu, L.J. Yu, L. Liu, 3D printing of Zr-based bulk metallic glasses and components for potential biomedical applications, *J. Alloys Compd.* 790 (2019) 963–973, doi:[10.1016/j.jallcom.2019.03.275](https://doi.org/10.1016/j.jallcom.2019.03.275).
- [48] J.P. Best, J. Ast, B. Li, M. Stolpe, R. Busch, F. Yang, X. Li, J. Michler, J.J. Kruzic, Relating fracture toughness to micro-pillar compression response for a laser powder bed additive manufactured bulk metallic glass, *Mater. Sci. Eng. A.* 770 (2020) 138535, doi:[10.1016/j.msea.2019.138535](https://doi.org/10.1016/j.msea.2019.138535).
- [49] L. Deng, A. Gebert, L. Zhang, H.Y. Chen, D.D. Gu, U. Kühn, M. Zimmermann, K. Kosiba, S. Pauly, Mechanical performance and corrosion behaviour of Zr-based bulk metallic glass produced by selective laser melting, *Mater. Des.* 189 (2020) 1–11, doi:[10.1016/j.matdes.2020.108532](https://doi.org/10.1016/j.matdes.2020.108532).
- [50] D. Ouyang, Q. Zheng, L. Wang, H. Wang, C. Yang, P. Zhang, N. Li, The brittleness of post-treatment of 3D printed Zr-based metallic glasses in supercooled liquid state, *Mater. Sci. Eng. A.* 782 (2020) 139259, doi:[10.1016/j.msea.2020.139259](https://doi.org/10.1016/j.msea.2020.139259).
- [51] Y. Zhang, X. Lin, X. Gao, X. Su, S. Guo, W. Huang, Crystallization behavior of $Zr_{55}Cu_{30}Al_{10}Ni_5$ amorphous alloys produced by selective laser melting of pre-annealed powders, *J. Alloys Compd.* 819 (2020) 153013, doi:[10.1016/j.jallcom.2019.153013](https://doi.org/10.1016/j.jallcom.2019.153013).
- [52] J. Shi, S. Ma, S. Wei, J.P. Best, M. Stolpe, A. Beckmann, S. Mostafavi, S. Korte-Kerzel, B. Markert, 3D pore structure characterization and hardness in a powder bed fusion-processed fully amorphous Zr-based bulk metallic glass, *Mater. Charact.* 162 (2020) 110178, doi:[10.1016/j.matchar.2020.110178](https://doi.org/10.1016/j.matchar.2020.110178).
- [53] S. Pauly, C. Schrickner, S. Scudino, L. Deng, U. Kühn, Processing a glass-forming Zr-based alloy by selective laser melting, *Mater. Des.* 135 (2017) 133–141, doi:[10.1016/j.matdes.2017.08.070](https://doi.org/10.1016/j.matdes.2017.08.070).
- [54] Y. Lu, H. Zhang, H. Li, H. Xu, G. Huang, Z. Qin, X. Lu, Crystallization prediction on laser three-dimensional printing of Zr-based bulk metallic glass, *J. Non. Cryst. Solids.* 461 (2017) 12–17, doi:[10.1016/j.jnoncrysol.2017.01.038](https://doi.org/10.1016/j.jnoncrysol.2017.01.038).
- [55] D. Ouyang, N. Li, W. Xing, J. Zhang, L. Liu, 3D printing of crack-free high strength Zr-based bulk metallic glass composite by selective laser melting, *Intermetallics* 90 (2017) 128–134, doi:[10.1016/j.intermet.2017.07.010](https://doi.org/10.1016/j.intermet.2017.07.010).
- [56] C. Yang, C. Zhang, W. Xing, L. Liu, 3D printing of Zr-based bulk metallic glasses with complex geometries and enhanced catalytic properties, *Intermetallics* 94 (2018) 22–28, doi:[10.1016/j.intermet.2017.12.018](https://doi.org/10.1016/j.intermet.2017.12.018).
- [57] D. Ouyang, N. Li, L. Liu, Structural heterogeneity in 3D printed Zr-based bulk metallic glass by selective laser melting, *J. Alloys Compd.* 740 (2018) 603–609, doi:[10.1016/j.jallcom.2018.01.037](https://doi.org/10.1016/j.jallcom.2018.01.037).
- [58] V. Pacheco, D. Karlsson, J.J. Marattukalam, M. Stolpe, B. Hjörvarsson, U. Jansson, M. Sahlberg, Thermal stability and crystallization of a Zr-based metallic glass produced by suction casting and selective laser melting, *J. Alloys Compd.* 825 (2020) 153995, doi:[10.1016/j.jallcom.2020.153995](https://doi.org/10.1016/j.jallcom.2020.153995).
- [59] J.J. Marattukalam, V. Pacheco, D. Karlsson, L. Riekehr, J. Lindwall, F. Forsberg, U. Jansson, M. Sahlberg, B. Hjörvarsson, Development of process parameters for selective laser melting of a Zr-based bulk metallic glass, *Addit. Manuf.* 33 (2020) 101124, doi:[10.1016/j.addma.2020.101124](https://doi.org/10.1016/j.addma.2020.101124).
- [60] N. Sohrabi, R.S. Panikar, J. Jhabvala, A.R. Buch, S. Mischler, R.E. Logé, Laser coating of a Zr-based metallic glass on an aluminum substrate, *Surf. Coatings Technol.* 400 (2020), doi:[10.1016/j.surfcoat.2020.126223](https://doi.org/10.1016/j.surfcoat.2020.126223).
- [61] N. Sohrabi, J. Jhabvala, G. Kurtuldu, M. Stoica, A. Parrilli, S. Berns, E. Polatidis, S. Van Petegem, S. Hugon, A. Neels, J.F. Löffler, R.E. Logé, Characterization, mechanical properties and dimensional accuracy of a Zr-based bulk metallic glass manufactured via laser powder-bed fusion, *Mater. Des.* 199 (2021) 109400, doi:[10.1016/j.matdes.2020.109400](https://doi.org/10.1016/j.matdes.2020.109400).
- [62] X. Lu, M. Nursulton, Y. Du, W. Liao, Structural and mechanical characteristics of $Cu_{50}Zr_{43}Al_{7}$ bulk metallic glass fabricated by selective laser melting, *Materials (Basel)* 12 (2019), doi:[10.3390/ma12050775](https://doi.org/10.3390/ma12050775).
- [63] X. Gao, Z. Liu, J. Li, E. Liu, C. Yue, K. Zhao, G. Yang, Selective laser melting of CuZr-based metallic glass composites, *Mater. Lett.* 259 (2020) 126724, doi:[10.1016/j.matlet.2019.126724](https://doi.org/10.1016/j.matlet.2019.126724).
- [64] L. Deng, S. Wang, P. Wang, U. Kühn, S. Pauly, Selective laser melting of a Ti-based bulk metallic glass, *Mater. Lett.* 212 (2018) 346–349, doi:[10.1016/j.matlet.2017.10.130](https://doi.org/10.1016/j.matlet.2017.10.130).
- [65] P. Fischer, A. Blatter, V. Romano, H.P. Weber, Selective laser sintering of amorphous metal powder, *Appl. Phys. A Mater. Sci. Process.* 80 (2005) 489–492, doi:[10.1007/s00339-004-3062-7](https://doi.org/10.1007/s00339-004-3062-7).
- [66] I. Yadroitsev, A. Gusarov, I. Yadroitsava, I. Smurov, Single track formation in selective laser melting of metal powders, *J. Mater. Process. Technol.* 210 (2010) 1624–1631, doi:[10.1016/j.jmatprotec.2010.05.010](https://doi.org/10.1016/j.jmatprotec.2010.05.010).
- [67] F. Bosio, A. Aversa, M. Lorusso, S. Marola, D. Gianoglio, L. Battezzati, P. Fino, D. Manfredi, M. Lombardi, A time-saving and cost-effective method to process alloys by Laser Powder Bed Fusion, *Mater. Des.* 181 (2019) 107949, doi:[10.1016/j.matdes.2019.107949](https://doi.org/10.1016/j.matdes.2019.107949).
- [68] J. Jhabvala, Study of the consolidation process under macro- and microscopic thermal effects in selective laser sintering and selective laser melting, *EPFL* (2010), doi:[10.5075/epfl-thesis-4609](https://doi.org/10.5075/epfl-thesis-4609).
- [69] S. Pogatscher, D. Leutenegger, A. Hagmann, P.J. Uggowitzer, J.F. Löffler, Characterization of bulk metallic glasses via fast differential scanning calorimetry, *Thermochim. Acta.* 590 (2014) 84–90, doi:[10.1016/j.tca.2014.06.007](https://doi.org/10.1016/j.tca.2014.06.007).
- [70] G. Kurtuldu, K.F. Shamlaye, J.F. Löffler, Metastable quasicrystal-induced nucleation in a bulk glass-forming liquid, *Proc. Natl. Acad. Sci.* 115 (2018) 6123–6128, doi:[10.1073/pnas.1717941115](https://doi.org/10.1073/pnas.1717941115).
- [71] S. Pogatscher, P.J. Uggowitzer, J.F. Löffler, In-situ probing of metallic glass formation and crystallization upon heating and cooling via fast differential scanning calorimetry, *Appl. Phys. Lett.* 104 (2014) 251908, doi:[10.1063/1.4884940](https://doi.org/10.1063/1.4884940).
- [72] F. Haag, S. Geisel, G. Kurtuldu, J.F. Löffler, Bulk metallic glass casting investigated using high-speed infrared monitoring and complementary fast scanning calorimetry, *Acta Mater.* 151 (2018) 416–423, doi:[10.1016/j.actamat.2018.02.029](https://doi.org/10.1016/j.actamat.2018.02.029).
- [73] F. Haag, R. Sauget, G. Kurtuldu, S. Prades-Rödel, J.E.K. Schawe, A. Blatter, J.F. Löffler, Assessing continuous casting of precious bulk metallic glasses, *J. Non. Cryst. Solids.* 521 (2019) 119120, doi:[10.1016/j.jnoncrysol.2018.09.035](https://doi.org/10.1016/j.jnoncrysol.2018.09.035).
- [74] G. Kurtuldu, J.F. Löffler, Multistep Crystallization and Melting Pathways in the Free-Energy Landscape of a Au–Si Eutectic Alloy, *Adv. Sci.* 7 (2020) 1903544, doi:[10.1002/advsc.201903544](https://doi.org/10.1002/advsc.201903544).
- [75] N. Sohrabi, J.E.K. Schawe, J. Jhabvala, J.F. Löffler, R.E. Logé, Critical crystallization properties of an industrial-grade Zr-based metallic glass used in additive manufacturing, *Scr. Mater.* 199 (2021) 113861, doi:[10.1016/j.scriptamat.2021.113861](https://doi.org/10.1016/j.scriptamat.2021.113861).
- [76] V. Gunenthiram, P. Peyre, M. Schneider, M. Dal, F. Coste, R. Fabbro, Analysis of laser-melt pool–powder bed interaction during the selective laser melting of a stainless steel, *J. Laser Appl.* 29 (2017) 022303, doi:[10.2351/1.4983259](https://doi.org/10.2351/1.4983259).
- [77] W. Ge, S. Han, Y. Fang, J. Cheon, S.J. Na, Mechanism of surface morphology in electron beam melting of Ti6Al4V based on computational flow patterns, *Appl. Surf. Sci.* 419 (2017) 150–158, doi:[10.1016/j.apsusc.2017.05.033](https://doi.org/10.1016/j.apsusc.2017.05.033).
- [78] C.L.A. Leung, S. Marussi, R.C. Atwood, M. Towrie, P.J. Withers, P.D. Lee, In situ X-ray imaging of defect and molten pool dynamics in laser additive manufacturing, *Nat. Commun.* 9 (2018) 1–9, doi:[10.1038/s41467-018-03734-7](https://doi.org/10.1038/s41467-018-03734-7).
- [79] A.M. Mancisidor, F. Garcandia, M.S. Sebastian, P. Álvarez, J. Díaz, I. Unanue, Reduction of the residual porosity in parts manufactured by selective laser melting using skywriting and high focus offset strategies, *Phys. Procedia.* 83 (2016) 864–873, doi:[10.1016/j.phpro.2016.08.090](https://doi.org/10.1016/j.phpro.2016.08.090).
- [80] Y. Tian, D. Tomus, P. Rometsch, X. Wu, Influences of processing parameters on surface roughness of Hastelloy X produced by selective laser melting, *Addit. Manuf.* 13 (2017) 103–112, doi:[10.1016/j.addma.2016.10.010](https://doi.org/10.1016/j.addma.2016.10.010).
- [81] J. Xie, A. Kar, J.A. Rothenflue, W.P. Latham, Temperature-dependent absorptivity and cutting capability of CO₂, Nd:YAG and chemical oxygen–iodine lasers, *J. Laser Appl.* 9 (1997) 77–85, doi:[10.2351/1.4745447](https://doi.org/10.2351/1.4745447).
- [82] U. Scipioni Bertoli, A.J. Wolfer, M.J. Matthews, J.-P.R. Delplanque, J.M. Schoenung, On the limitations of Volumetric Energy Density as a design parameter for Selective Laser Melting, *Mater. Des.* 113 (2017) 331–340, doi:[10.1016/j.matdes.2016.10.037](https://doi.org/10.1016/j.matdes.2016.10.037).
- [83] K.G. Prashanth, S. Scudino, T. Maity, J. Das, J. Eckert, Is the energy density a reliable parameter for materials synthesis by selective laser melting? *Mater. Res. Lett.* 5 (2017) 386–390, doi:[10.1080/21663831.2017.1299808](https://doi.org/10.1080/21663831.2017.1299808).
- [84] W.E. King, H.D. Barth, V.M. Castillo, G.F. Gallegos, J.W. Gibbs, D.E. Hahn, C. Kamath, A.M. Rubenchik, Observation of keyhole-mode laser melting in laser powder-bed fusion additive manufacturing, *J. Mater. Process. Technol.* 214 (2014) 2915–2925, doi:[10.1016/j.jmatprotec.2014.06.005](https://doi.org/10.1016/j.jmatprotec.2014.06.005).
- [85] A.M. Rubenchik, W.E. King, S.S. Wu, Scaling laws for the additive manufacturing, *J. Mater. Process. Technol.* 257 (2018) 234–243, doi:[10.1016/j.jmatprotec.2018.02.034](https://doi.org/10.1016/j.jmatprotec.2018.02.034).
- [86] T. DebRoy, H.L. Wei, J.S. Zuback, T. Mukherjee, J.W. Elmer, J.O. Milewski, A.M. Beese, A. Wilson-Heid, A. De, W. Zhang, Additive manufacturing of metallic components – Process, structure and properties, *Prog. Mater. Sci.* 92 (2018) 112–224, doi:[10.1016/j.pmatsci.2017.10.001](https://doi.org/10.1016/j.pmatsci.2017.10.001).
- [87] A. Otto, A. Patschger, M. Seiler, Numerical and experimental investigations of humping phenomena in laser micro welding, *Phys. Procedia.* 83 (2016) 1415–1423, doi:[10.1016/j.phpro.2016.09.004](https://doi.org/10.1016/j.phpro.2016.09.004).
- [88] M. Kuno, *Thermodynamics of the Pd₄₃Ni₁₀Cu₂₇P₂₀ Metallic Glass-Forming Alloy*, Oregon State University, 2001.
- [89] Y. Shen, Y. Li, C. Chen, H.L. Tsai, 3D printing of large, complex metallic glass structures, *Mater. Des.* 117 (2017) 213–222, doi:[10.1016/j.matdes.2016.12.087](https://doi.org/10.1016/j.matdes.2016.12.087).
- [90] M. Yamauchi, T. Tsukuda, Production of an ordered (B2) CuPd nanoalloy by low-temperature annealing under hydrogen atmosphere, *Dalt. Trans.* 40 (2011) 4842–4845, doi:[10.1039/C0DT01632B](https://doi.org/10.1039/C0DT01632B).
- [91] N. Wanderka, E. Davidov, G. Miehe, V. Naundorf, M.P. Macht, J. Banhart, Crystallization of Pd₄₀Cu₃₀Ni₁₀P₂₀ Bulk Glass, *J. Metastable Nanocrystalline Mater.* 20–21 (2004) 35–40, doi:[10.4028/www.scientific.net/jmmn.20-21.35](https://doi.org/10.4028/www.scientific.net/jmmn.20-21.35).
- [92] D.L. Jaeger, S. Mridha, D. Choudhuri, Sundeep R. Banerjee, Compositional Analysis of as-cast and Crystallized Pd₄₃Cu₂₇Ni₁₀P₂₀ Bulk Metallic Glass, *Microsc. Microanal.* 20 (2014) 814–815, doi:[10.1017/S1341927614005790](https://doi.org/10.1017/S1341927614005790).
- [93] C. Ma, N. Nishiyama, A. Inoue, Phase equilibria and thermal stability of Pd–Cu–Ni–P alloys, *Mater. Trans.* 43 (2002) 1161–1165, doi:[10.2320/matertrans.43.1161](https://doi.org/10.2320/matertrans.43.1161).
- [94] Y. Li, Y. Shen, C. Chen, M.C. Leu, H.L. Tsai, Building metallic glass structures on crystalline metal substrates by laser-foil-printing additive manufacturing, *J. Mater. Process. Technol.* 248 (2017) 249–261, doi:[10.1016/j.jmatprotec.2017.05.032](https://doi.org/10.1016/j.jmatprotec.2017.05.032).
- [95] N. Nishiyama, A. Inoue, Glass-forming ability of Pd_{42.5}Cu₃0Ni_{7.5}P₂₀ alloy with a low critical cooling rate of 0.067K/s, *Appl. Phys. Lett.* 80 (2002) 568–570, doi:[10.1063/1.1445475](https://doi.org/10.1063/1.1445475).
- [96] J. Schroers, W.L. Johnson, R. Busch, Crystallization kinetics of the bulk-glass-forming melt, *Appl. Phys. Lett.* 1158 (2001) 1–4.
- [97] L.-R. Lu, G.P. Görlner, R. Willnecker, H.J. Fecht, Investigation on the Thermal Stability of Bulk Glass Forming Alloy Pd–Cu–Ni–P, *MRS Proc.* 644 (2000) L3.2, doi:[10.1557/PROC-644-L3.2](https://doi.org/10.1557/PROC-644-L3.2).
- [98] J.L. Soubeyroux, N. Claret, Crystallisation behaviour of bulk metallic glasses by in-situ neutron diffraction, *Appl. Phys. A.* 74 (2002) s1025–s1027, doi:[10.1007/s003390101181](https://doi.org/10.1007/s003390101181).

- [99] J. Schroers, Y. Wu, R. Busch, W.L. Johnson, Transition from nucleation controlled to growth controlled crystallization in $\text{Pd}_{43}\text{Ni}_{10}\text{Cu}_{27}\text{P}_{20}$ melts, *Acta Mater* 49 (2001) 2773–2781, doi:[10.1016/S1359-6454\(01\)00159-8](https://doi.org/10.1016/S1359-6454(01)00159-8).
- [100] J.E.K. Schawe, J.F. Löffler, Existence of multiple critical cooling rates which generate different types of monolithic metallic glass, *Nat. Commun.* 10 (2019) 1–10, doi:[10.1038/s41467-018-07930-3](https://doi.org/10.1038/s41467-018-07930-3).
- [101] J. Ma, K.C. Chan, L. Xia, S.H. Chen, F.F. Wu, W.H. Li, W.H. Wang, Multi-layer laminated Pd-based metallic glass with enhanced plasticity, *Mater. Sci. Eng. A* 587 (2013) 240–243, doi:[10.1016/j.msea.2013.08.043](https://doi.org/10.1016/j.msea.2013.08.043).
- [102] G. Kumar, S. Prades-Rodel, A. Blatter, J. Schroers, Unusual brittle behavior of Pd-based bulk metallic glass, *Scr. Mater.* 65 (2011) 585–587, doi:[10.1016/j.scriptamat.2011.06.029](https://doi.org/10.1016/j.scriptamat.2011.06.029).
- [103] F.H. Dalla Torre, A. Dubach, J. Schällibaum, J.F. Löffler, Shear striations and deformation kinetics in highly deformed Zr-based bulk metallic glasses, *Acta Mater* 56 (2008) 4635–4646, doi:[10.1016/j.actamat.2008.05.021](https://doi.org/10.1016/j.actamat.2008.05.021).
- [104] W. Li, Y. Gao, H. Bei, Instability analysis and free volume simulations of shear band directions and arrangements in notched metallic glasses, *Sci. Rep.* 6 (2016) 1–11, doi:[10.1038/srep34878](https://doi.org/10.1038/srep34878).
- [105] A.S. Argon, M. Salama, The mechanism of fracture in glassy materials capable of some inelastic deformation, *Mater. Sci. Eng.* 23 (1976) 219–230, doi:[10.1016/0025-5416\(76\)90198-1](https://doi.org/10.1016/0025-5416(76)90198-1).